Anthropogenic CO_2 changes in the Equatorial Atlantic Ocean

Fajar N. M.[1], Guallart E. F.[2], Steinfeldt R.[3], Ríos A. F.[1], Pelegrí J. L[2]., Pelejero C.[2, 4], Calvo E.[2], Pérez F. F.[1*]

[1]Instituto de Investigacións Mariñas – Consejo Superior de Investigaciones Científicas, IIM-CSIC, Eduardo Cabello 6, E-36208 Vigo, Spain.

[2]Institut de Ciències del Mar – Consejo Superior de Investigaciones Científicas, Passeig Marítim de la Barceloneta 37-49, E-08003 Barcelona, Spain.

[3]Institut für Umweltphysik, Abt. Ozeanographie, Universität Bremen, Otto-Hahn-Allee, 28359 Bremen, Germany

[4]Institució Catalana de Recerca i Estudis Avançats, Passeig Lluís Companys 23, E-08010 Barcelona, Spain.

Corresponding author[*]:

Tel: +34 986 231 930 (Ext. 360); Fax: +34 986 292 762

E –mail address: fiz.perez@iim.csic.es (F. F. Pérez)

Abstract

Methods based on CO_2 and CFC data are used to describe and evaluate the anthropogenic CO_2 (C_{ant}) concentrations, C_{ant} specific inventories and C_{ant} storage rates in the Equatorial Atlantic Ocean. The C_{ant} variability in the water masses is evaluated from the comparison of two hydrographic sections along 7.5ºN, carried out in 1993 and 2010. During both cruises, high C_{ant} concentrations are detected in the upper layers, with values decreasing progressively towards the deep layers. Overall, the C_{ant} concentrations increase from 1993 to 2010, with a large increment in the upper North Atlantic Deep Water layer, of about 0.18 ± 0.03 $\mu mol \cdot kg^{-1} \cdot y^{-1}$. In 2010, the C_{ant} inventory along the whole section amounts to 58.9 ± 2.2 and 45.1 ± 2.0 $mol \cdot m^{-2}$ using CO_2 and CFC based methods, respectively, with most C_{ant} accumulating in the western basin. Considering the time elapsed between the two cruises, C_{ant} storage rates of 1.01 ± 0.18 and 0.75 ± 0.17 $mol \cdot m^{-2} \cdot y^{-1}$ (CO_2 and CFC based methods, respectively) are obtained. Below ~1000 m, these rates follow the pace expected from a progressive increase of C_{ant} at steady state; above ~1000 m, C_{ant} increases faster, mainly due to the retreat of the Antarctic Intermediate Waters.

Keywords

Anthropogenic CO_2, inventories, storage rate, Equatorial Atlantic Ocean

1. Introduction

Since the beginning of the industrial revolution, humankind has emitted large quantities of CO_2 into the atmosphere (Le Quéré et al., 2009), rising global atmospheric CO_2 concentrations from 280 ppm, at the start of industrial revolution, to nearly ~ 400 ppm by the end of 2013 (Tans and Keeling, 2014). This increase has been mainly caused by the anthropogenic release of CO_2 to the atmosphere from fossil fuel combustion, deforestation and other land-use change activities. The fuel combustion has become the dominant source of anthropogenic emissions to the atmosphere since around 1920 (Le Quéré et al., 2013). Only a portion of the CO_2 emitted to the atmosphere is accumulated there, as nearly 55% of the anthropogenic CO_2 (C_{ant}) is taken up by the ocean and the terrestrial biosphere (Ballantyne et al., 2012; Le Quéré et al., 2009). On-going efforts

are being made to quantify the magnitude of these two sinks with high accuracy. Model results, for example, constrain the mean CO_2 uptake rates of the land and the ocean to 2.9±0.8 and 2.6±0.5 $PgC \cdot yr^{-1}$, respectively, for the period 2004-2013 (Le Quéré et al., 2014). Over the last 200 years, the ocean has acted as a growing net CO_2 sink (Gruber et al., 2009). There is evidence suggesting that the oceanic uptake fraction, the net CO_2 emissions taken up by the ocean, was possibly lower during 1980 - 2005 (37 ± 7%) as compared to 1750 - 1994 (42 ± 7%) (Sabine et al., 2004), even though the uncertainty in the estimates is larger than the difference between them. This decrease in the fraction of ocean uptake may be related to the increase in the terrestrial sink (Ciais et al. 2013). Also this decrease in the oceanic uptake fraction is consistent with the current understanding that the ocean CO_2 sink is limited by the transport rate of CO_2 from the surface to the deep ocean (Zeebe, 2012). It is also in agreement with the known nonlinearity of the carbonate chemistry, according to which the CO_2 uptake capacity of seawater is reduced as its CO_2 concentration increases (Zeebe and Wolf-Gladrow, 2001).

In order to better constrain the oceanic CO_2 budget, oceanographers have focused on separating the C_{ant} signal from the natural CO_2. However, estimating the anthropogenic component of the total inorganic carbon (C_T) is a difficult task because C_{ant} cannot be directly measured and its signal in the ocean is only a small perturbation (on the order of a few per cent at most) on the natural background distribution of CO_2. In the late seventies, several studies used different calculations based on total alkalinity (A_T), C_T and dissolved oxygen measurements to estimate the C_{ant} concentration ([C_{ant}]), the so-called back-calculation techniques. Since the first approaches by Brewer (1978) and Chen and Millero (1979), several authors have tried to improve the methods for estimating C_{ant} [ΔC^* (Gruber et al., 1996), LM05 (Lo Monaco et al., 2005), TrOCA (Touratier et al., 2007) or φC_T^0 (Vázquez-Rodríguez et al., 2009a)], all of them with strengths and weaknesses (van Heuven et al., 2011). In addition, other C_{ant} estimation techniques use tracers such as chlorofluorocarbons (CFCs), for example the Transit Time Distribution (TTD) (Waugh et al., 2004, 2006) or the "short-cut method" (Thomas and Ittekkot, 2001), and other authors estimate C_{ant} using multiple linear regression approaches (MLR and eMLR) based on independent chemical and hydrographic parameters (Friis et al., 2005; Tanhua et al., 2007; Wanninkhof et al., 2010). Khatiwala et al. (2013) suggested that a combination of C_{ant} estimation methods is necessary to

achieve a robust quantification of the C_{ant} ocean sink. In the present study, two methods are used to estimate the [C_{ant}] in the Equatorial Atlantic Ocean: the φC_T^0 method based on CO_2 data and the TTD method based on CFC data.

The interplay of air-sea exchange processes and ocean circulation in the winter mixed layer (WML) determines the properties of a water mass, such as salinity, temperature, preformed components of nutrient salts, and tracers of atmospheric origin. These properties are subsequently transported into the ocean interior, where they mix with other water parcels from different winter mixing layers. Hence, the local water mass properties at any point in the interior are determined considering the different transit times since the different water parcels last contacted the surface. The back-calculation techniques assume a steady-state (SS) of the ocean properties, which allows calculating the biological impact in the carbon cycle from the oxygen and nutrient observations, with the empirical relationship in the preformed C_T and A_T in the WML. Also, the SS of the ocean properties is the underlying assumption of the MLR methods when using a single parametrization that fits the natural C_T between cruises (Plancherel et al. 2014). The TTD method (Waugh et al. 2004) and Green's function method (Khatiwala et al. 2009) also assumes a SS in the ocean transport that permits linking each point of the ocean with the surface. Moreover, based on earlier studies of transient tracers (Keeling and Bolin, 1967; Broecker et al., 1979), Holfort et al. (1998), Rosón et al. (2003) and Alvarez et al. (2003) determined the volumetrically-integrated C_{ant} storage rate proportionally to the temporal increase of [C_{ant}] in the WML. Tanhua et al., (2007) infers the C_{ant} inventories in subtropical North Atlantic from the decadal C_{ant} storage rate computed using eMLR and assuming SS. Previously, Tanhua et al. (2006) from a comparison of the observed changes in C_T and CFC fields with those predicted from an eddy-permitting ocean circulation model, found that C_{ant} is in transient SS in the North Atlantic. This means that C_{ant} increases over time through the whole water column in a manner that is proportional to the time-dependent of [C_{ant}] in the WML. Hence, [C_{ant}] changes for a given time period can be determined from [C_{ant}] considering the exponential fit $[C_{ant}] = Ae^{\lambda t}$, that describes the history of atmospheric CO_2 and [C_{ant}] in the ocean surface WML since the Industrial Revolution (Tanhua et al., 2007; Steinfeldt et al., 2009; Khatiwala et al., 2013; Pérez et al., 2013). Under a SS approximation, the time derivative of [C_{ant}] (C_{ant} storage rate) can be calculated multiplying the inventory of [C_{ant}] by the annual growth rate (λ), i.e. SS_ΔC_{ant} rate = $\lambda \cdot [C_{ant}]$. Steinfeldt et al. (2009)

reported an annual increase rate of 1.69% for the factor λ. Based on the variability estimated in the [C_{ant}] increase in the surface, the uncertainty associated to λ was found to be 0.10 %.

Historically, and because of its important role in deep water formation, the northern North Atlantic region has been far more sampled than the tropics. Nonetheless, it is of crucial importance to expand our knowledge from subpolar to tropical regions to better understand the dynamics and biogeochemical characteristics of the whole North Atlantic Ocean. In terms of C_{ant}, there are several works on the Atlantic Ocean that include C_{ant} estimations in the Equatorial Atlantic (Lee et al., 2003; Steinfeldt et al., 2009; Vázquez-Rodríguez et al., 2009b; Ríos et al., 2010; Wanninkhof et al., 2010), although none of them described the variability of the C_{ant} storage rate along this equatorial region. Inverse estimates of the atmospheric CO_2 absorption by the global ocean found considerable C_{ant} uptake in the equator and the tropics (Mikaloff Fletcher et al., 2006), favoured by the low Revelle factors of tropical and subtropical warm waters that facilitate the absorption of atmospheric C_{ant}. However, Lee et al. (2003) reported relatively small total and specific inventories in the tropical Atlantic. The absorbed C_{ant} at these low latitudes appears to be mostly advected northward along the surface with low depth penetration. In fact, the tropical Atlantic is the main contributor to North Atlantic C_{ant} storage associated with the upper limb of the overturning circulation (Álvarez et al., 2003). Taking into account the role of the oceanic circulation in the distribution of C_{ant} between basins and the potential temporal change of the C_{ant} storage at regional scales (Gruber et al., 1996), a reassessment of the C_{ant} storage rates and the specific inventories in different oceanic regions is necessary to better constrain how the ocean carbon cycle evolves on decadal scales in the face of climate change.

The 7.5ºN section is situated in a dynamically complex area (Figure 1) characterized by currents flowing mainly in the zonal direction: the North Equatorial (NEC) and the South Equatorial (SEC) currents (branches of the subtropical gyres), which are separated by the eastward Equatorial Undercurrent (EUC), the North Equatorial Countercurrent (NECC), and the North Equatorial Undercurrent (NEUC). The structure and variability of all of them are largely driven by the wind field over the tropical Atlantic, in particular by the variability and/or movement of the Intertropical Convergence Zone (ITCZ) (Stramma and Schott, 1999; Urbano et al., 2008; Rosell-

Fieschi et al., 2015). In the western basin the section is situated two to three degrees to the north of the NEUC (Arhan et al., 1998), while in the eastern basin, it lays in the southern margin of the Guinea Dome (Brandt et al., 2010).

The vertical thermohaline structure of the 7.5ºN section is characterized by six main water masses (Figure 2), which are used here to divide the section into density layers. The surface is dominated by the South Atlantic Central Water (SACW) (Stramma and England, 1999; Stramma and Schott, 1999), which is formed in the confluence zone of the Brazil and Falkland currents. The SACW is transported within the South Atlantic Current (SAC) until it flows into the SEC. The Sub-Antarctic Mode Water (SAMW) extends from near the surface to more than 600 m depth (Herraiz-Borreguero and Rintoul, 2011). The SAMW is formed in the South Atlantic, at about 40ºS, and is transported by the anti-cyclonic circulation in the South Atlantic subtropical gyre (Tsuchiya et al., 1994). The Antarctic Intermediate Water (AAIW) spans around 1000 m of depth (Murata et al., 2008), originating from subduction of surface waters in the northern Drake Passage and the Falkland Current loop (Stramma and England, 1999; Stramma and Schott, 1999). The North Atlantic Deep Water (NADW), located between 1200 and 4500 m, is formed by the confluence of deep waters formed in the Nordic and Labrador Seas and then is transported towards the equator by the Deep Western Boundary Current (DWBC) (Steinfeldt et al., 2007). Finally, the bottom waters are characterized by the Antarctic Bottom Water (AABW) (Rhein et al., 1998), formed by the confluence of water masses originating in different locations around Antarctica (Johnson, 2008), are exported northward and ventilate the ocean's bottom layer.

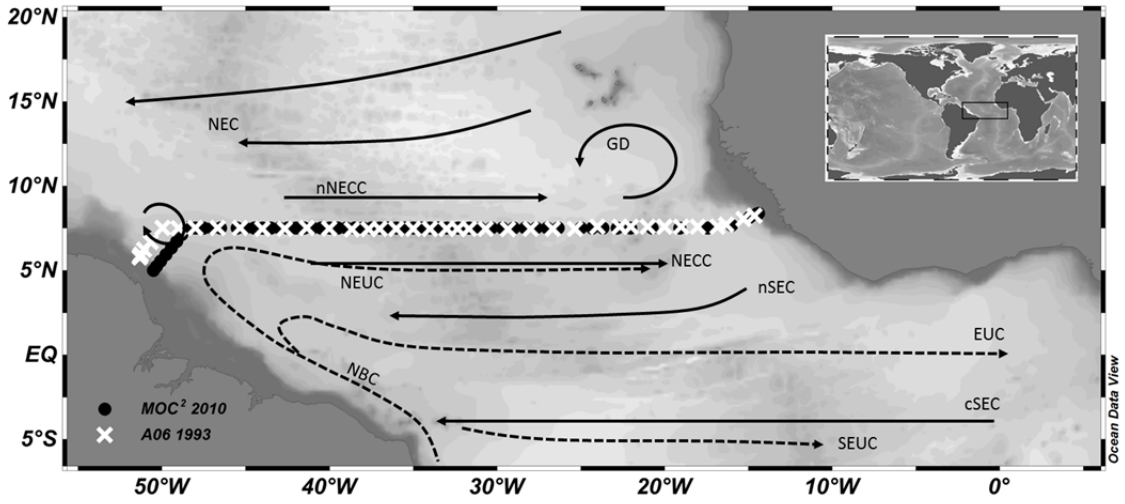

Figure 1. Stations of the A06 cruise of 1993 (black dots) and MOC2 cruise of 2010 (white crosses) along 7.5°N, together with a schematic diagram of the shallow circulation in the Subtropical and Tropical Atlantic. Surface (black solid arrows) and thermocline (black dashed arrows). Currents shown are the North Equatorial Current (NEC), the north and central South Equatorial Current (nSEC, cSEC), the North Equatorial Countercurrent (NECC), the North Brazil Current (NBC), the North and South Equatorial Under Current (NEUC, SEUC), the Equatorial Under Current (EUC), and the cyclonic circulation around the Guinea Dome (GD) [Adapted from Brandt et al. (2012, 2010)].

Recent studies have demonstrated the existence of substantial changes in the Atlantic Meridional Overturning Circulation (AMOC) at the equatorial Atlantic Ocean (San Antolín Plaza et al., 2012; Hernández-Guerra et al., 2014), mostly affecting the AAIW and uNADW. These changes in circulation, together with the high increase of C_{ant} between 1989 and 2005 in the South Atlantic as compared with the North Atlantic (Wanninkhof et al., 2010), suggest the existence of major processes that affect C_{ant} in the equatorial Atlantic Ocean. Our objective is to use the two occupations of the 7.5°N section in order to assess the changes in C_{ant} in the Equatorial North Atlantic between 1993 and 2010. The section is divided in different layers according to the main water masses present in the section and further splitting them in different zonal regions, according to the hydrographic features and bathymetry. The C_{ant} specific inventories are computed and the C_{ant} storage rates are evaluated and compared to the expected rates under the assumption of a steady state.

2. Data and methodology

2.1 Cruises

In 2010, the MOC2-Equatorial cruise (hereinafter MOC2) sailed the 7.5ºN section eastward, following the same route as the first WOCE A06 cruise (hereinafter A06) in 1993. The section extends from the north-eastern coast of South America, at ~ 51.3ºW, to the western coast of Central Africa, at ~14.4ºW (Figure 1).

MOC2 in 2010

The MOC2 2010 cruise was carried out on board the Spanish R/V Hespérides from April to May 2010 (Ríos et al., 2012a), completing 59 full depth CTD casts (Figure 1). The distance between stations was 30 nautical miles from the coast of South America to the Mid-Atlantic Ridge (MAR), and ~60 nautical miles from the MAR to the African coast. A SBE911plus CTD probe was used for the station-based profiling of the water column. The CTD unit was equipped with temperature and conductivity sensors and a SBE-43 oxygen probe. The rosette was equipped with 24 Niskin bottles of 12 L. At each station, samples for dissolved oxygen (O_2), inorganic nutrients, A_T and pH were taken at 24 depths throughout the whole water column, and samples of C_T were taken at four depth levels. Water samples in glass ampoules for the analyses of CFCs were drawn at least at every second station.

Samples of inorganic nutrients, O_2, A_T and pH were analysed on board, while C_T samples were poisoned with 300 µL of saturated $HgCl_2$ and stored in darkness until their analysis in the CO_2 lab of the Marine Research Institute (IIM-CSIC) in Vigo (Spain). The O_2 measurements were performed following the modified Winkler method (Culberson, 1991) with a potentiometric titration, where the O_2 content of the sample is transformed to iodine and titrated with thiosulfate afterwards. The samples of A_T were analysed by an endpoint method using an automatic potentiometric titrator with a combined glass electrode (Mintrop et al., 2000), in which the titration was carried out using two pH endpoints (Pérez and Fraga, 1987). The seawater pH measurements were obtained on the total scale using the spectrophotometric method described by Clayton and Byrne (1993), adding m-cresol purple as an indicator and controlling the temperature at 25ºC with a thermostatic bath, and introducing a correction of +0.0047 pH units (DelValls and Dickson, 1998). The C_T samples were measured using a

SOMMA (Single-Operator Multiparameter Metabolic Analyzers) system, where an aliquot of 20 mL is acidified with H_3PO_4 in a glass stripping chamber and the formed CO_2 gas is carried into a coulometric cell by a CO_2-free gas (N_2), where the titration is performed (Johnson et al., 1993). Both A_T and C_T measurements were calibrated with CO_2 certified reference material (CRM) provided by Dr. Andrew Dickson (Scripps Institute of Oceanography). Since C_T was not measured at all levels of the water column, it was calculated from A_T and pH data using the thermodynamic equations of the carbonate system and the CO_2 dissociation constants from Mehrbach et al. (1973), refitted by Dickson and Millero (1987).

The good agreement between the measured and calculated C_T is evidenced by their linear fit, yielding a correlation coefficient (R^2) of 0.998 (Ríos et al., 2012a) with a slope of 1.0005 ± 0.006 and a mean difference of 2.8 ± 3.9 $\mu mol \cdot kg^{-1}$ (n=43). The secondary quality control (2^{nd} QC), i.e. the crossover analysis method (Key et al., 2010; Tanhua et al., 2010) was applied to MOC2 data (O_2, pH, A_T and C_T, phosphate (PO_4^{3-}) and nitrate (NO_3^-)) for waters deeper than 3500 m, where the long term changes are minimal or within the analytical method uncertainties. Only PO_4^{3-} and NO_3^- needed to be bias-adjusted by multiplicative factors of 1.03 and 1.01, respectively, while the remaining parameters showed offsets indistinguishable from zero within the CARINA and GLODAP uncertainties (Tanhua et al., 2010), further attesting the good quality of the data. The CFC ampoules were flame sealed on board and then sent to the tracer lab at the University of Bremen, where they were measured with a gas chromatographic system as described in Bulsiewicz et al. (1998). The detection limit is 0.003 $pmol \cdot kg^{-1}$ for both CFC-11 and CFC-12, and the accuracy is 2% or 0.008 $pmol \cdot kg^{-1}$, whichever is greater. All data were compiled and are available at the CLIVAR and Carbon Hydrographic Data Office (CCHDO) (http://cchdo.ucsd.edu/cruise/29HE20100405).

A06 in 1993

In February – March 1993, the Cither-I cruise (WOCE A06 line) was carried out along the parallel 7.5°N on board the French R/V L'Atalante (Oudot, 1993). CTD profiles of potential temperature (θ), salinity (S) and O_2 (Arhan et al., 1998) were obtained at each station, separated ~30 nautical miles except over the continental slopes, where spacing was reduced to 10-20 nautical miles (Oudot et al., 1998). The rosette was equipped with 32 Niskin bottles of 8 L. Samples for O_2, nutrients, CFC-11 and CFC-12 samples were

234 also taken in each station along the cruise (Andrié et al., 1998). In addition, pH and C_T
235 samples were taken every two stations and analysed on board (Oudot and Ternon, 1994;
236 Oudot et al., 1995; Ternon et al., 2001). pH was measured at 25ºC and based on the total
237 hydrogen ion concentration scale (pH_{T25}), using a Ross combination electrode calibrated
238 with Tris buffer, and C_T samples were analysed by gas chromatography (Oudot and
239 Ternon, 1994; Oudot et al., 1995; Ternon et al., 2001). The poor quality and noise of the
240 C_T data prevented their inclusion in the GLODAP global compilation (Wanninkhof et
241 al., 2003). The original pH data of the A06 1993 cruise used by Ternon et al. (2001),
242 together with the remaining hydrographic and biogeochemical data, including CFC-11
243 and CFC-12, are available at the CCHDO.

244 The θ, S, nutrients and O_2 data were corrected following the recommendations of
245 Gouretski and Jancke (2000) and their confidence was confirmed by application of the
246 crossover analysis (Key et al., 2010; Tanhua et al., 2010). The pH data set was reported
247 to CCHDO at seawater scale and in situ temperature ($pH_{SWSinsitu}$) (Oudot and Ternon,
248 1994; Ternon et al., 2001). Hence, as it is described in Oudot and Ternon (1994), we
249 reverted the equations to transform the reported $pH_{SWSinsitu}$ into the initially measured
250 pH_{T25} (Gieskes, 1969; Millero, 1979), and finally, they were rescaled to pH_{SWS25} (van
251 Heuven et al., 2009). A 2nd QC was applied finding only a positive bias of 0.007 pH
252 units east of the MAR, which was corrected in the present work by adding -0.007 units.
253 In order to estimate [C_{ant}], A_T and C_T are needed. Thus, a 3D moving window
254 multilinear regression algorithm (Velo et al., 2013) was used to estimate the A_T data.
255 This algorithm was developed to fill gaps in the A_T of the CARINA and GLODAP data
256 collections for the Atlantic Ocean, generating values with estimated uncertainties of
257 about 6 µmol·kg^{-1}. Afterwards, C_T was computed using pH_{SWS25} and A_T, and the
258 dissociation constants of Mehrbach et al. (1973) refitted by Dickson & Millero (1987).
259 Finally, a last 2nd QC was used to verify the confidence of A_T and C_T data (Tanhua et al.
260 2010), obtaining a mean offset of 0.8 ± 1.6 and 1.1 ± 3.3 µmol·kg^{-1}, respectively (see
261 Appendix A for details).

262 2.2 Regions and water mass layers of the 7.5°N section

263 The 7.5ºN section was divided into two basins and two regions each, and six vertical
264 density layers (Figure 2).

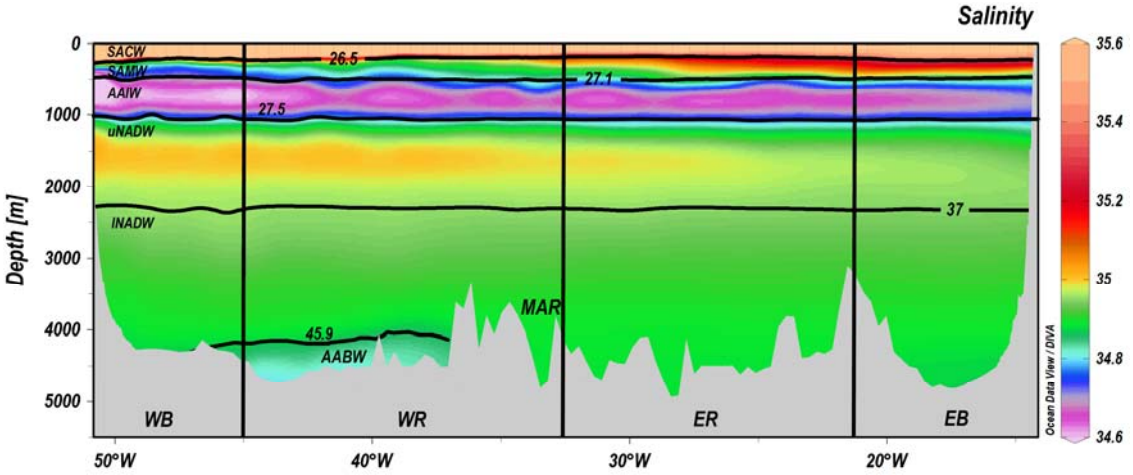

Figure 2. Vertical distribution of salinity along the 7.5°N section in 2010 (MOC2). Vertical black lines mark the division into regions: The Western Boundary (WB) and Western Ridge (WR) regions are located westward of the Mid-Atlantic Ridge while the Eastern Ridge (ER) and Eastern Boundary (EB) regions are located eastward. Black horizontal lines correspond to the isopycnals used to separate the section into different layers, according to the water mass properties. From the sea surface toward deep-waters, the reference density levels are σ_0=26.5, σ_0=27.1, σ_0=27.5, σ_2=37 and σ_4=45.9; subscripts 0, 2 and 4 refer to the reference pressure of 0, 2000 and 4000 dbar, respectively

The western and eastern basins are divided by the MAR, located at about 32.5ºW. Westward of the MAR, the Western Boundary (WB) region extends from the coast of Guiana (~ 50ºW) to 45ºW, enclosing the region of most AAIW and NADW influence, and the Western Ridge (WR) region, from 45ºW to 32.5ºW, where the AABW signal is most evident. Eastward of the MAR, we differentiated the Eastern Ridge (ER) region, from 32.5ºW to 21ºW (Sierra Leone ridge), and the Eastern Boundary (EB) region, from 21ºW to the African coast (~ 15ºW), in order to distinguish between the Gambia abyssal plain and the Sierra Leone basin (Arhan et al., 1998). The density layers were selected according to the main water masses present in the Equatorial Atlantic Ocean (Tsuchiya et al., 1994; Arhan et al., 1998; Stramma and England, 1999; Stramma and Schott, 1999; Mémery et al., 2000; Brea et al., 2004; Sarafanov et al., 2007; Murata et al., 2008; Herraiz-Borreguero and Rintoul, 2011).

The upper layer is dominated by the SACW, from the sea surface to the isopycnal σ_0 = 26.5 kg·m^{-3} (Stramma and Schott, 1999). The SACW in this region is characterised by θ >14ºC and salinities of 34.8-36.8. The SAMW layer is enclosed between σ_0 = 26.5 and σ_0 = 27.1 kg·m^{-3} (Mémery et al., 2000) and contains all waters with θ between 7 and 15ºC and salinities between 34.7 and 35.9. The SACW and SAMW are the components of the permanent thermocline, which includes waters warmer than 8ºC. The third layer

corresponds to the AAIW, which includes waters in the density range $27.1 \leq \sigma_0 \leq 27.5$ $kg \cdot m^{-3}$ (Murata et al., 2008). The potential temperature varies between 4 and 9ºC and the salinity shows the minimum values of the water column at 7.5ºN, between 34.5 and 34.9. In the deep waters, NADW is split into upper NADW (uNADW) and lower NADW (lNADW). The uNADW layer incorporates waters with densities between $\sigma_0 =$ 27.5 $kg \cdot m^{-3}$ and $\sigma_2 = 37$ $kg \cdot m^{-3}$ (Murata et al., 2008), mainly including Labrador Sea Water (LSW) that is easily identified by a relative deep maximum signal in salinity about 34.7-35.0 and θ between ~ 3 and 5ºC in this region. The lNADW layer is delimited by $\sigma_2 = 37.0$ $kg \cdot m^{-3}$ and $\sigma_4 = 45.9$ $kg \cdot m^{-3}$ (Johnson, 2008) and it is characterized by waters progressively colder (~ 2-3ºC) than uNADW. The AABW layer encloses waters below $\sigma_4 = 45.9$ $kg \cdot m^{-3}$ (Rhein et al., 1998; Sarafanov et al., 2007) . AABW is characterized by low salinity values of 34.8 - 34.9, coincident with the coldest waters (< 2°C) at 7.5ºN. The mean θ and S values for each layer and region are detailed in the Appendix B for 1993 and Appendix C for 2010.

Table 1. Minima and maxima potential temperature (θ) and salinity (S) values for the characteristic water masses at 7.5°N in 1993 and 2010: South Atlantic Central Water (SACW), SubAntartic Mode Water (SAMW), Antarctic Intermediate Water (AAIW), upper North Atlantic Deep Water (uNADW), lower North Atlantic Deep Water (lNADW) and Antarctic Bottom Water (AABW). The last column shows the isopycnals used to define the layers corresponding to those water masses.

Water mass layer	S		Θ (ºC)		σ ($kg \cdot m^{-3}$)
	1993	2010	1993	2010	
SACW	35.1-36.8	34.8-36.6	14.2-27.6	14.1-30.1	$\sigma_0 < 26.5$
SAMW	34.7-35.9	34.7-35.9	7.3-15.2	7.7-15.5	$26.5 < \sigma_0 < 27.1$
AAIW	34.5-34.8	34.5-34.9	4.6-7.9	4.7-8.6	$27.1 < \sigma_0 < 27.5$
uNADW	34.7-35.0	34.8-35.0	2.8-5.1	2.9-5.0	$\sigma_0 > 27.5$ and $\sigma_2 < 37$
lNADW	34.9-35.0	34.9-35.0	1.8-3.0	1.8-2.9	$\sigma_2 > 37$ and $\sigma_4 < 45.9$
AABW	34.8-34.9	34.8-34.9	1.1-1.9	1.1-1.8	$\sigma_4 > 45.9$

The salinity distribution for 2010 (Figure 2) shows its highest values along the SACW layer and progressively decreases with depth along the SAMW layer until a minimum at about 800 m that represents the core of AAIW. In deeper waters (~1700 m), the relative maximum in salinity identifies the uNADW layer. The S values decrease again with depth in the lNADW until they reach the characteristic relative minimum of the AABW.

2.3 C_{ant} estimations

The $[C_{ant}]$ estimations were obtained for the A06 (1993) and MOC2 (2010) data sets by applying both the φC_T^0 (Vázquez-Rodríguez et al., 2009a, 2012) and the TTD method

(Waugh et al., 2006; Steinfeldt et al., 2009). Hereinafter, we differentiate between C_{ant}-φC_T^0 and C_{ant}-TTD according to the method used to estimate the [C_{ant}].

The φC_T^0 method (Vázquez-Rodríguez et al., 2009a, 2012) is a back-calculation approach oriented to estimate C_{ant} from the comparison of modern C_T concentrations with estimates of their preindustrial reference concentrations, under the assumption that biogeochemical processes that modulate oceanic C_T have operated invariably with time. It shares principles with the classical ΔC^* method, but proposes different parameterizations to calculate the air-sea disequilibrium (ΔC_{dis}) and the preformed alkalinity (A_T^0) to assess the contribution of $CaCO_3$ dissolution to C_T. A relevant aspect of these parameterizations is that they rely on conservative properties of the subsurface layer (100-200 m), which is taken as record for characterizing WML properties (Vázquez-Rodríguez et al., 2012). These parameters are obtained from subsurface data and applied directly to calculate [C_{ant}] in waters above the 5ºC isotherm, and estimated by means of an extended Optimum MultiParameter (eOMP) analysis for cold deep waters (< 5ºC). This procedure especially improves the C_{ant} estimations in cold deep waters involved in complex mixing processes between northern and southern hemispheric water masses. An uncertainty of ±5.2 $\mu mol \cdot kg^{-1}$ was calculated by the random propagation of the errors for the φC_T^0 method (Vázquez-Rodríguez et al., 2009a). The φC_T^0 C_{ant} estimations at 7.5ºN for 1993 and 2010 are shown in Figure 3 (a,b).

The TTD method is an indirect method that uses measurements of transient tracers (e.g., CFCs) to estimate C_{ant} without using carbon data. The basis of the TTD method, developed by Waugh et al. (2004), is that the only information necessary to estimate C_{ant} is the knowledge about the time-dependant evolution of C_{ant} in the surface ocean, and the rate at which this surface boundary condition is transported and mixed into the ocean´s interior. This is done by means of particular transfer functions (here called TTDs) that try to represent the water mass age distribution within the ocean interior, according to the measured tracer data. It is assumed that the transport is steady and that TTDs can be modelled as Inverse Gaussian functions (Waugh et al., 2004). Thus, C_{ant} is determined from the difference between C_T at the time of the water masses is formed, as deduced from the age distribution, and C_T in the preindustrial, and assuming a preindustrial atmospheric CO_2 concentration of 280 ppm (Waugh et al., 2004). To

calculate the water mass age distribution, it is necessary to know their atmospheric time histories (Walker et al., 2000) and their solubility functions (Warner and Weiss, 1985). As in Steinfeldt et al. (2009), it is assumed that the surface waters are in equilibrium, e.g. their CFC saturation is 100%, whereas this saturation is smaller for the formation of deep water masses (e,g, 85% for uNADW and 65% for lNADW and AABW). For the A06 cruise, both CFC-11 and CFC-12 data were used, and C_{ant} is inferred from the TTD resulting from the mean age of both tracers. For the MOC2 cruise, only CFC-12 data have been used to infer the TTDs for two reasons: First, the CFC-11 peak in the chromatogram of flame sealed samples that have been stored for a longer time, is overlaid by a negative signal, which makes the determination of the peak area more difficult. Second, CFC-11 has increased in the atmosphere only until 1994, in contrast to CFC-12 which had concentrations growing until 2003. It is not possible to derive a unique mean age for very young waters from CFC-11 data in 2010, as waters formed at the end of the 1980s and after 2000 have the same CFC-11 concentration. The uncertainty of the TTD approach evaluated by Waugh et al. (2006) is ±6 $\mu mol \cdot kg^{-1}$ for individual C_{ant} estimations. The TTD C_{ant} estimations at 7.5ºN for 1993 and 2010 are shown in Figure 3 (c, d).

2.4 C_{ant} changes, C_{ant} specific inventories and C_{ant} storage rates

Considering the selected regions and layers along the 7.5ºN, the mean values of S, θ, A_T, C_T, C_{ant}-φC_T^0 and C_{ant}-TTD, together with the standard error of their means ($x \pm \varepsilon$), were calculated for 22 regional layers (boxes) from the 1993 and 2010 datasets (Appendix B and C, respectively). The uncertainty of the mean ($\varepsilon=\sigma/\sqrt{n}$) was determined from the standard deviation (σ) of the samples (n) in each box, including a randomly propagated error in each sample due to the C_{ant} method uncertainty. The thickness of each layer (within each region) was computed as the average vertical distance between layers weighted by the separation between stations, and normalised to obtain the identical water column depth in the four regions of both cruises taking the 2010 MOC2 cruise water column depth as reference (see Appendix B).

Considering these mean values, the C_{ant} changes (ΔC_{ant}-φC_T^0 and ΔC_{ant}-TTD) between 1993 and 2010 were calculated as the difference between the values of [C_{ant}] in 2010 minus those in 1993 (Table 2), together with the differences in S and θ (ΔS and Δθ,

respectively - Figure 4). The annual C_{ant} changes and the associated uncertainties, ΔC_{ant}-φC_T^0 and ΔC_{ant}-TTD rates ($\mu mol \cdot kg^{-1} \cdot y^{-1}$), were calculated as $\Delta X = 1/17 * [(X_{2010} - X_{1993}) \pm \sqrt{[(\varepsilon_{2010})^{2+} (\varepsilon_{1993})^2]})]$ (Table 2), where X and ε are given in Appendices B and C. In order to visualize the spatial distribution of the changes at 7.5ºN, additional calculations were necessary because the 1993 and 2010 datasets do not have the same stations grid. More specifically, the 2010 bottle grid was used as the reference grid into which the bottle data in 1993 was interpolated using a Delaunay triangulation. In this way, a C_{ant} profile for 1993 was obtained at the 2010 positions. The differences between the 2010 and the 1993 profiles represent the ΔC_{ant}-φC_T^0 and ΔC_{ant}-TTD, respectively (Figure 5).

In each region, the C_{ant} specific inventory (iC_{ant}, $mol \cdot m^{-2}$) was calculated for either method as the sum of the mean [C_{ant}] of each layer multiplied by its thickness. The iC_{ant} was also calculated for the western basin (WB+WR), the eastern basin (ER+EB) and for the whole 7.5ºN basin (50ºW-15ºW). In order to calculate the iC_{ant} errors, an uncertainty between 0 and the maximum standard error of the mean value of [C_{ant}] was assigned to the [C_{ant}] values, and the iC_{ant} was recalculated a hundred times. Hence, the iC_{ant} errors are the standard deviation of these one hundred calculations. Both the iC_{ant}-φC_T^0 and iC_{ant}-TTD values together with their errors are shown in Table 3.

The annual C_{ant} storage rates in $mol \cdot m^{-2} \cdot y^{-1}$ were calculated from the difference between $iC_{ant1993}$ and $iC_{ant2010}$ (Table 4). Both sets of C_{ant} storage rates were calculated for the section and they were also obtained for the western and eastern basins and *upper* (including SACW, SAMW and AAIW) and *lower* (including uNADW, lNADW and AABW) layers (Table 4). Furthermore, the *observed* C_{ant} storage rates were compared to the *expected* rates assuming a steady state (SS) of the C_{ant} distributions (SS_C_{ant}-φC_T^0 and SS_C_{ant}-TTD rates). The SS_ΔC_{ant} rates ($\mu mol \cdot kg^{-1} \cdot y^{-1}$) were calculated (Table 2) as the product between $\lambda = 0.0169 \pm 0.001 y^{-1}$ and the averaged [C_{ant}] between 1993 and 2010 (Appendices B and C) for each of the 22 boxes. Subsequently, the *expected* SS_C_{ant} storage rate ($mol \cdot m^{-2} \cdot y^{-1}$) was calculated for the whole section and their *upper* and *lower* layer in the western and eastern basins (Table 4).

3. Results and Discussion

3.1 Distribution of C_{ant}-φC_T^0 and C_{ant}-TTD

The vertical distributions of [C_{ant}-φC_T^0] and [C_{ant}-TTD] show similar patterns along the 7.5ºN section in 1993 (Figure 3a, c) and 2010 (Figure 3b, d). High [C_{ant}] values are found in the upper layers, from where the signal decreases until a minimum within the AAIW layer, at about 1000 m depth. A relatively high C_{ant} signal is observed in the uNADW. A second [C_{ant}] minimum is present at the upper boundary of the lNADW, where levels are close to the uncertainty of both methods and similar to the minimum within the AAIW. Towards the bottom, in the lower part of the lNADW layer, [C_{ant}] increases slightly. Below 1000 m, there is a general horizontal gradient of [C_{ant}] with the western basin presenting values higher [C_{ant}] than in the eastern one, likely due to the transport of more recently ventilated water masses by the DWBC, close to the western margin of the Atlantic Ocean (Steinfeldt et al., 2007). The main difference in the vertical structure between [C_{ant}-φC_T^0] and [C_{ant}-TTD] is the vertical gradient in the upper 1000 m, sharper for the TTD method, which results in a smaller [C_{ant}-TTD] for AAIW. Another difference for both the 1993 and the 2010 distributions is the westward increase of [C_{ant}] in the uNADW, more pronounced for the TTD method, with a distinct maximum in the WB region in 2010. The mean and standard deviation of the differences found by the φC_T^0 and the TTD methods (C_{ant}-φC_T^0 - C_{ant}-TTD) are 1.7±2.4 µmol·kg^{-1} in 1993 and 2.7±4.2 µmol·kg^{-1} in 2010, which indicates that there is a good agreement between the two methods, illustrated by a very high correlation (r^2 = 0.98 for 1993 and r^2 = 0.97 for 2010; Appendices B and C).

The SACW layer presents the maximum [C_{ant}-φC_T^0] for the whole section (Figure 3a, c), with mean values in the WR region increasing from 53.4±0.7 µmol·kg^{-1} in 1993 to 69.8±0.7 µmol·kg^{-1} in 2010 (Appendices B and C, respectively). The [C_{ant}-TTD] in the WR region is almost identical, with values changing from 54.2±0.6 µmol·kg^{-1} (1993) to 72.0±1.7 µmol·kg^{-1} (2010). Regarding the SAMW layer, there is a noticeable penetration of the C_{ant}-φC_T^0 from 1993 to 2010 (Figure 3a, c). Regardless of the method used, the isolines 30 and 40 µmol·kg^{-1} moved down from SACW to SAMW layers. The mean values of [C_{ant}-φC_T^0] range between 18.8±0.9 µmol·kg^{-1} (WR) and 22.1±1.3 µmol·kg^{-1} (EB) in 1993, and between 31.0±0.9 µmol·kg^{-1} (WB) and 35.0±1.9 µmol·kg^{-1} (EB) in 2010. The mean values of [C_{ant}-TTD] and [C_{ant}-φC_T^0] are very similar in the

SAMW layer, with values varying from 18.0±0.7µmol·kg^{-1} (WR) and 21.2±0.9 µmol·kg^{-1} (WB) in 1993, and between 26.7±1.1 µmol·kg^{-1} (WB) and 33.7±1.5 µmol·kg^{-1} (EB) in 2010 (Appendices B and C). In the AAIW layer, both methods exhibit a clear minimum horizon during both cruises, more extreme and wider in 1993 than in 2010. This thinning of the C_{ant} signal in 2010 is due to the mixing/dilution of the AAIW with C_{ant}-loaded surrounding waters, which generate an increase of C_{ant}. This finding agrees with the fact that the northward flow of AAIW was less intense in 2010 than in 1993 (San Antolín Plaza et al., 2012; Hernández-Guerra et al., 2014). The AAIW layer displays lower values for [C_{ant}-TTD] than for [C_{ant}-φC_T^0], especially in 2010. The [C_{ant}-φC_T^0] reveals a homogenous longitudinal distribution with mean values around 6 µmol·kg^{-1} in 1993, and around 15 µmol·kg^{-1} in 2010 (Figure 3a, b), with the exception of WB region in 1993 that shows a mean [C_{ant}-φC_T^0] of 9.8±0.7 µmol·kg^{-1}. The [C_{ant}-TTD] shows a higher gradient toward the western basin, varying from 7.2±0.4 µmol·kg^{-1} (WB) to 3.6±0.2 µmol·kg^{-1} (EB) in 1993 and from 8.3±0.6 µmol·kg^{-1} (WB) to 5.6±0.6 µmol·kg^{-1} (EB) in 2010 (Figure 3c, d).

The important difference in C_{ant} between both cruises within the AAIW stratum has also been recently noticed by Guallart et al. (2014) along 24.5ºN. In that study, the authors suggested that, regarding the C_{ant} computation in the AAIW layer, it is important to consider that methods based on CO_2 measurements are particularly sensitive to changes in that water mass. The φC_T^0 method is strongly linked to natural processes through the Redfield ratios (Vázquez-Rodríguez et al., 2009a), which in these regions are influenced by the presence of the oxygen minimum zone (OMZ) (Stramma et al., 2008). Additionally, the high C_{ant} increase found for the South Atlantic Ocean (Wanninkhof et al., 2010) could explain the relatively high [C_{ant}-φC_T^0] in waters with southern origin. It should also be noticed that the TTD method does not always detect the same C_{ant} as φC_T^0 (Tanhua et al., 2007). In old water masses that have been in equilibrium with an atmosphere previous to 1960, C_{ant}-φC_T^0 could exhibit values higher than C_{ant}-TTD, because at that time the atmospheric concentration of CFCs was very low.

In the deep layers, the most remarkable structure is the signal of the LSW (the main component of the uNADW), which is associated to a tongue of relatively high values of [C_{ant}] during both cruises (Figure 3). According to Lazier et al. (2002), the early 1990s were a period of exceptionally intense convection, which created a fresher deep pool of

LSW. Significant decreases in salinity are detected in the WB and WR regions, where LSW spreads. Further, the eastward recirculation of the NADW (Arhan et al., 1998; Mémery et al., 2000) would have promoted the extension of the LSW signal into the eastern regions in 2010, as the results using either the φC_T^0 or TTD methods suggest (Figure 3b, d) for the uNADW layer. In 1993, the LSW signal is mainly restricted to the western regions (WB and WR), where there are some bowls of uNADW with [C_{ant}-φC_T^0] and [C_{ant}-TTD] slightly higher than 10 µmol·kg^{-1}, with mean [C_{ant}-φC_T^0] and [C_{ant}-TTD] values of 8.9±0.3 and 8.5±0.2 µmol·kg^{-1} in the WB region, respectively. In 2010, not only the western basin but also the ER region exhibit [C_{ant}-φC_T^0] > 10 µmol·kg^{-1}, with a mean [C_{ant}-φC_T^0] of 9.2±0.3 µmol·kg^{-1}. However, the [C_{ant}-TTD] values are significantly lower than [C_{ant}-φC_T^0] in the ER and EB regions during both cruises.

The lNADW layer shows the lowest values of C_{ant} of the whole section in both cruises, rarely reaching values above 10 µmol kg^{-1} (Figure 3b, d). In this layer, the TTD approach detects lower (higher) concentrations in the eastern (western) regions than the φC_T^0 method, with estimates more homogenous throughout the section (Figure 3). The average [C_{ant}-φC_T^0] in the lNADW ranges from 5.4±0.2 µmol·kg^{-1} in the WB in 1993 to 8.2±0.3 µmol·kg^{-1} in the EB in 2010, and the mean [C_{ant}-TTD] values are between 2.9±0.1 µmol·kg^{-1} in the EB in 1993 and 10.7±0.3 µmol·kg^{-1} in the WB in 2010. Once again, the pulse of LSW in the early 1990's (Lazier et al., 2002), together with the eastward branching of the DWBC (Mémery et al., 2000) and the northward cyclonic flow of the NADW into the south-eastern part of the Gambia Basin reported by Sarafanov et al. (2007), could be the processes responsible for the C_{ant} redistribution in the ER region observed during 2010. Nevertheless, no pattern could be easily described there because our estimates of [C_{ant}] were within the methodology uncertainty. The AABW layer is located at the bottom of the WB and WR (Figure 3). In 1993, the mean [C_{ant}-φC_T^0] ranged between 4.8±0.4 µmol·kg^{-1} (WB) and 7.7±0.2 µmol·kg^{-1} (WR), while in 2010 the concentrations are slightly higher: 7.2±0.3 µmol·kg^{-1} in the WB and 8.8±0.2 µmol·kg^{-1} in the WR. The TTD approach leads to similar estimates of mean [C_{ant}-TTD], between 5.0±0.1 µmol·kg^{-1} (WR) and 7.3±0.1 µmol·kg^{-1} (WB) in 1993 and between 6.7±0.1 µmol·kg^{-1} (WR) and 9.0±0.4 µmol·kg^{-1} (WB) in 2010.

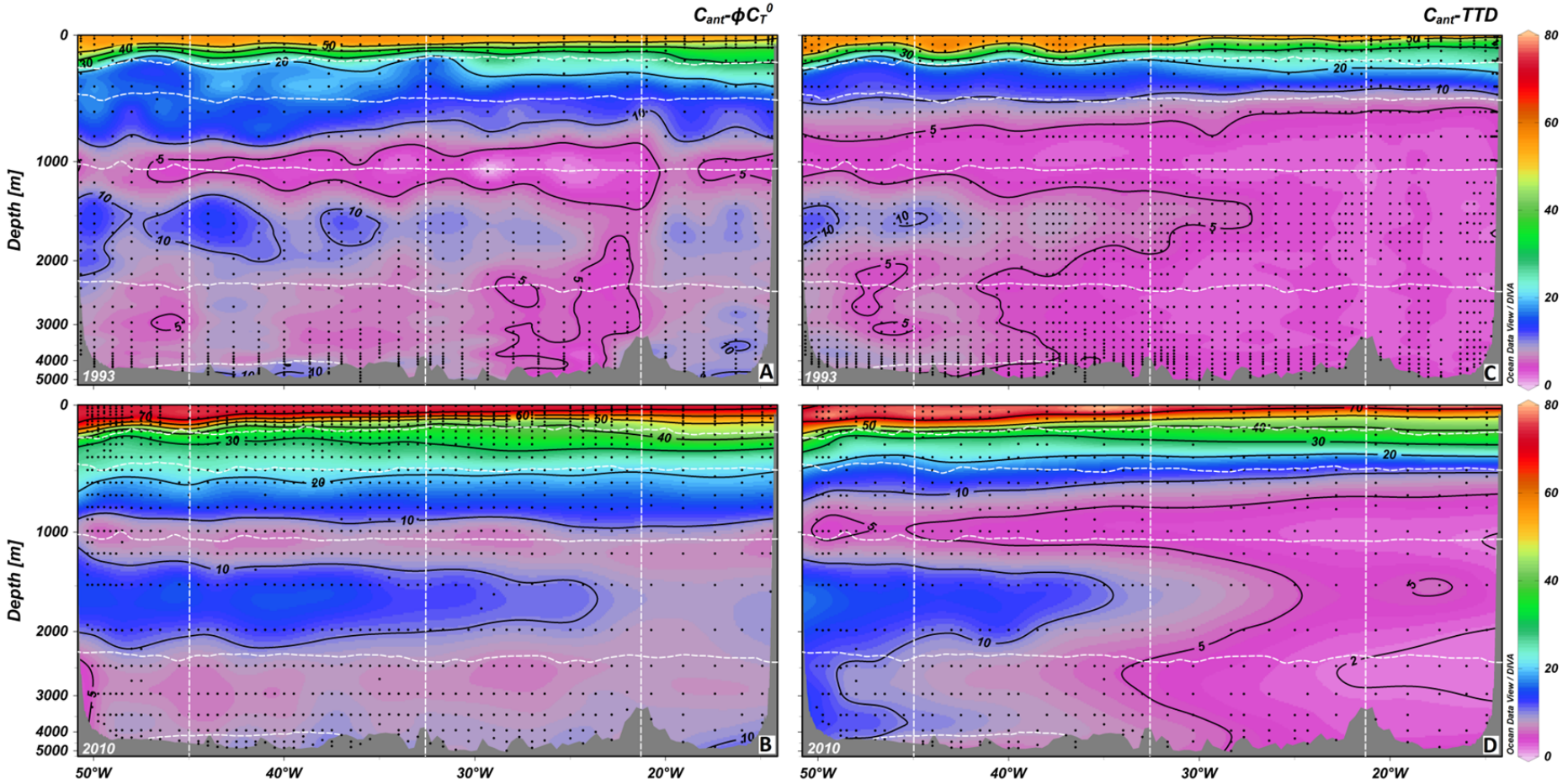

505

506 Figure 3. Distribution of C_{ant}-ϕC_T^0 and C_{ant}-TTD (μmol·kg^{-1}) along the 7.5°N section in 1993 (a, c) and 2010 (b, d). (a) and (b) panels show the profiles of C_{ant}-ϕC_T^0 while (c) and
507 (d) panels show the profiles of TTD-C_{ant} . The horizontal white dashed lines mark the layers and the vertical white dashed lines mark the regions.

3.2 Thermohaline changes

The A06 and MOC2 cruises were carried out in different seasons, being A06 a boreal winter cruise while MOC2 was a boreal spring cruise. The seasonality in the position of the ITCZ leads to changes in the tropical North Atlantic circulation (Rosell-Fieschi et al., 2015). One major change is the formation of the NECC, which begins in May in the EB and advances west until joining with the North Brazil Current (NBC) by July. Hence, the greatest changes in the thermohaline properties took place in the uppermost layers (SACW, SAMW) (Table 2, Figure 4). In general, S diminishes from 1993 to 2010 within the SACW layer of all regions, associated to a decrease in temperature in the regions close to the MAR, probably related to the different seasons when the cruises were carried out. However, in the WB, the SACW layer shows higher temperatures and lower salinities in 2010 than in 1993, which are likely due to the closer proximity of the stations to the Amazon River in 2010 (Figure 1). In the SAMW layer, it is worth highlighting the influence of the strong NBC seasonality in the WB, driving less saline and relative colder waters in 2010 than in 1993. In the remaining regions, both the salinity and temperature show a slight increment (Figure 4). In the case of the AAIW layer, $\Delta\theta$ and ΔS are positive (2010 properties higher than in 1993), with a slight trend to increasing $\Delta\theta$ eastwards (Figure 4) in agreement with the lower northward advection of AAIW in 2010 (San Antolín Plaza et al., 2012; Hernández-Guerra et al., 2014). In 2010, the uNADW layer was slightly fresher and warmer and the lNADW layer showed small changes, being saltier and warmer (Figure 4 and Table 2). Finally, AABW showed a slight decrease in θ and S in 2010 (together with an increment in SiO_2, from $[SiO_2]_{1993}$ = 43.1±0.8 to $[SiO_2]_{2010}$ = 47.5±2.6 $\mu mol \cdot kg^{-1}$ in the WB and $[SiO_2]_{1993}$ = 62.4±1.3 to $[SiO_2]_{2010}$ = 66.1±1.4 $\mu mol \cdot kg^{-1}$ in the WR). These findings suggest an increase of AABW and a decrease of lNADW what would agree with the weakening of the southward advection lNADW in 2010 (Hernández-Guerra et al (2014).

Table 2. Changes (± standard deviation) in potential temperature (θ, °C), salinity (S), C_{ant}-ϕC_T^0 (µmol·kg^{-1}) and C_{ant}-TTD (µmol·kg^{-1}) for each region and layer. ΔC_{ant} = $C_{ant2010}$-$C_{ant1993}$. The ΔC_{ant} annual rates (± standard error of mean) and SS_ΔC_{ant} rates (calculated as the averaged C_{ant} in 1993 and 2010 multiplied by 0.0169 y^{-1}) (µmol·kg^{-1}·y^{-1}) were calculated using the ϕC_T^0 and TTD methods. Italic fonts stand for values not significantly different from zero (p-level>0.05).

Region	Layer	ΔS	ΔΘ	ΔC_{ant} ϕC_T^0	ΔC_{ant} TTD	ΔC_{ant} ϕC_T^0 rate	[a]SS_ΔC_{ant} ϕC_T^0 rate	[b]ΔC_{ant} TTD rate	[a]SS_ΔC_{ant} TTD rate
WB	SACW	-0.227±0.286	*0.30±3.5*	16.4±6.6	17.8±6.5	0.96±0.06	1.04 (0.2)	1.05±0.11	1.07 (0.8)
	SAMW	-0.136±0.346	*-0.75±2.5*	10.2±6.4	6.7±6.6	0.60±0.09	0.44 (0.10)	0.39±0.11	0.42 (0.8)
	AAIW	*0.014±0.093*	*0.21±1.28*	5.6±6.2	*1.4±5.3*	0.33±0.06	0.21 (0.05)	*0.08±0.04*	0.13 (0.2)
	uNADW	-0.028±0.100	*0.23±1.02*	2.0±4.6	2.6±5.3	0.11±0.03	0.17 (0.08)	0.15±0.04	0.16 (0.8)
	lNADW	*0.003±0.027*	*0.09±0.45*	1.9±3.5	3.4±3.6	0.11±0.02	0.11 (0.9)	0.20±0.02	0.15 (0.01)
	AABW	-0.010±0.012	*-0.05±0.08*	2.4±1.9	1.7±1.5	0.14±0.03	0.10 (0.2)	0.10±0.02	0.14 (0.15)
WR	SACW	-0.100±0.213	*0.47±4.1*	13.4±10.4	19.0±7.8	0.79±0.11	0.98 (0.08)	1.12±0.11	1.06 (0.6)
	SAMW	*0.040±0.240*	*0.49±1.75*	13.1±9.0	8.7±6.3	0.77±0.06	0.43 (<0.001)	0.51±0.08	0.38 (0.10)
	AAIW	*0.012±0.061*	0.33±1.14	8.5±6.7	2.6±5.1	0.50±0.06	0.18 (<0.001)	0.15±0.03	0.11 (0.2)
	uNADW	-0.016±0.061	0.30±0.74	3.0±5.3	2.9±4.6	0.18±0.03	0.15 (0.2)	0.17±0.03	0.13 (0.10)
	lNADW	0.006±0.022	0.11±0.45	1.8±3.2	2.2±4.6	0.11±0.01	0.11 (0.6)	0.13±0.01	0.10 (0.02)
	AABW	-0.008±0.025	*-0.05±0.29*	1.2±2.7	1.7±2.4	0.07±0.02	0.14 (<0.001)	0.10±0.01	0.10 (1.0)
ER	SACW	-0.198±0.248	*-1.0±5.2*	11.0±8.5	12.9±8.1	0.65±0.09	0.98 (0.001)	0.76±0.19	0.92 (0.4)
	SAMW	*-0.011±0.201*	*0.01±1.8*	13.6±7.9	6.9±6.7	0.80±0.09	0.47 (<0.001)	0.41±0.15	0.41 (1.0)
	AAIW	0.023±0.080	0.42±1.28	8.7±5.6	2.5±3.8	0.51±0.06	0.18 (<0.001)	0.15±0.04	0.09 (0.12)
	uNADW	-0.007±0.067	0.23±0.69	2.4±5.0	1.5±4.4	0.14±0.02	0.13 (0.5)	0.09±0.02	0.07 (0.4)
	lNADW	0.006±0.021	0.09±0.39	1.2±3.1	0.6±1.1	0.07±0.01	0.12 (<0.001)	0.04±0.01	0.06 (0.10)
EB	SACW	*0.000±0.184*	*-0.03±4.9*	12.7±7.3	17.2±9.6	0.75±0.11	0.93 (0.11)	1.01±0.25	0.86 (0.6)
	SAMW	*0.027±0.165*	*0.22±1.72*	12.9±5.9	15.3±6.0	0.76±0.13	0.48 (0.05)	0.90±0.11	0.44 (<0.001)
	AAIW	*0.015±0.063*	*0.45±1.19*	8.8±4.6	2.0±3.3	0.52±0.07	0.18 (<0.001)	0.12±0.04	0.08 (0.3)
	uNADW	*-0.010±0.047*	*0.17±0.60*	*0.6±4.0*	*0.6±3.2*	*0.03±0.03*	0.13 (<0.001)	*0.04±0.04*	0.05 (0.8)
	lNADW	*0.000±0.028*	*0.02±0.36*	*-0.4±3.2*	*-0.5±3.1*	*-0.03±0.02*	0.14 (<0.001)	-0.03±0.01	0.04 (<0.001)

[a]) Grey boxes stand for values significantly different from the values of ΔC_{ant} located on the left (p-level <0.05 at 95%, given between parenthesis)

[b]) Grey boxes stand for values of ΔC_{ant} - ϕC_T^0 and ΔC_{ant} -TTD rates that are different (p-level<0.05 at 95%)

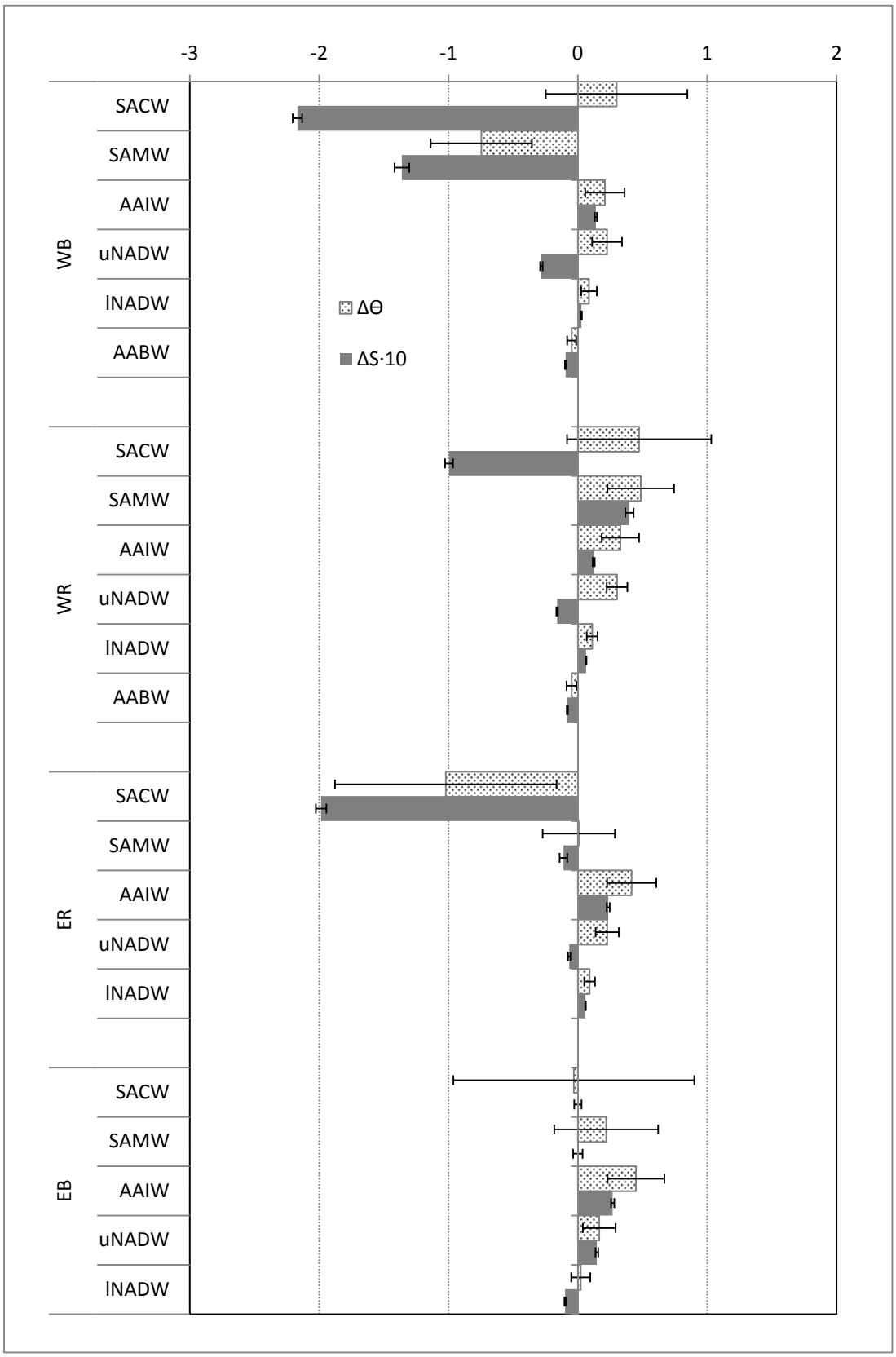

Figure 4. Changes in potential temperature (Δθ, °C, dotted bars) and salinity, (ΔS, 0.1, grey bars) calculated as the difference between MOC2 (2010) minus A06 (1993) for each region and layer. Note that ΔS is multiplied by 10 in order to have comparable scales. Error bar represent the standard error of the mean.

3.3 Changes in C_{ant} distribution

The distribution of ΔC_{ant}-φC_T^0 and ΔC_{ant}-TTD indicates a clear C_{ant} increase from 1993 to 2010 in the upper and eastward parts of the section (Figure 5). The SACW layer presents the largest increase in [C_{ant}-φC_T^0], around 14 µmol·kg^{-1} on average, with the highest ΔC_{ant}-φC_T^0 (16.4±6.6 µmol·kg^{-1}) in WB (Table 2). These values are even slightly higher in the case of ΔC_{ant}-TTD, with an average increase of about 17 µmol·kg^{-1} along the whole layer, and the highest ΔC_{ant}-TTD (19.0±6.5 µmol·kg^{-1}) found in the WR region. Regarding the SAMW layer, there is a homogenous high C_{ant} increase with ΔC_{ant}-φC_T^0 between 10.2±6.4µmol·kg^{-1} (WR) and 13.6±7.9 µmol·kg^{-1} (ER). The ΔC_{ant}-TTD ranges between 6.7±6.6 µmol·kg^{-1} (WR) and 15.3±6.0 µmol·kg^{-1} (EB). Throughout the AAIW layer, ΔC_{ant}-φC_T^0 values of around 5-10 µmol·kg^{-1} are observed, while ΔC_{ant}-TTD is significantly lower (close to 2 µmol·kg^{-1}; Figure 5). The difference in the ΔC_{ant} magnitude restates the different sensitivity of the φC_T^0 and TTD methods, as reported previously.

In deep waters, there is a good agreement between the φC_T^0 and TTD methods, which show C_{ant} changes lower than 4 µmol·kg^{-1} (Table 3) and a higher ΔC_{ant} in the western section and closer to MAR regions (Figure 5). According to the eastward spread of the high [C_{ant}] tongue and its mixing with less C_{ant}-loaded waters (i.e., less ventilated waters) (Steinfeldt et al., 2007) (Figure 3), the greater changes are located in the uNADW layer, with the highest ΔC_{ant}-φC_T^0 of 3.0 µmol·kg^{-1} (WR). Regarding the ΔC_{ant}-TTD, the largest change is found in the WB region of the lNADW. It is worth to remark that in deep and bottom waters, with [C_{ant}] values close to the uncertainty of the methodology, the differences in the concentrations could only be detected above the methodological noise when studying time periods of more than three decades (Ríos et al., 2012b).

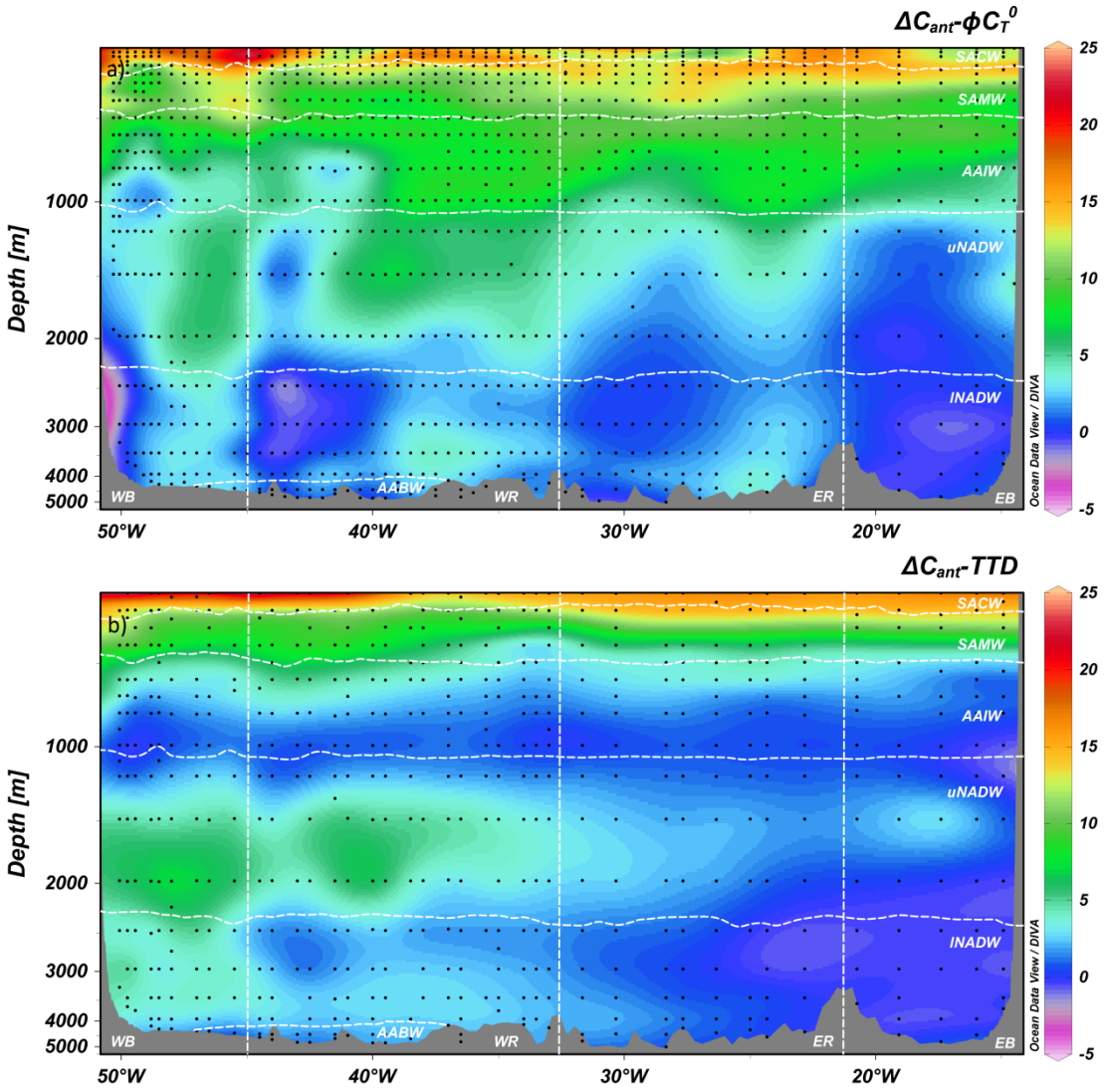

Figure 5. Distribution of ΔC_{ant}-ϕC_T^0 (a) and ΔC_{ant}-TTD (b) along the 7.5°N section, where ΔC_{ant}= $C_{ant2010}$-$C_{ant1993}$. The dots represent the sampling locations during the 2010 cruise. A Delaunay triangulation was used to calculate these C_{ant} differences. The position and depth of the MOC[2] stations (2010) were used as the reference grid and the data of A06 (1993) were interpolated into that grid.

In order to evaluate the annual changes, ΔC_{ant} rates are calculated for each of the 22 boxes (Table 2). According to the C_{ant} changes previously described, both the ΔC_{ant}-φC_T^0 and ΔC_{ant}-TTD rates are higher in the surface layer and they progressively decrease with depth, with similarities and differences always within uncertainties. In the SACW, the ΔC_{ant}-φC_T^0 and ΔC_{ant}-TTD rates show a very similar increase of C_{ant} in the WB and ER regions, while in WR and EB the ΔC_{ant}-TTD rates are larger than those detected with the φC_T^0 method. The ΔC_{ant}-φC_T^0 rates are generally higher than the ΔC_{ant}-TTD rates in the SAMW, with the exception of EB, which displays a lower rate. The ΔC_{ant}-φC_T^0 rates of the AAIW layer show a C_{ant} increase clearly higher than the

584 ΔC_{ant}-TTD rates in the whole section. However those differences seem to disappear in
585 deep waters, particularly in the uNADW layer, where the ΔC_{ant} rates estimated with the
586 φC_T^0 and TTD methods agree in their values. The ΔC_{ant}-TTD rates are in general a bit
587 higher in the lNADW than the rates from the ΔC_{ant}-φC_T^0, with the only exception of the
588 ER, where the ΔC_{ant}-φC_T^0 rate shows a slightly higher rate. Regarding the AABW, both
589 ΔC_{ant}-φC_T^0 and ΔC_{ant}-TTD display similar rates.

590 The absolute values of the differences between ΔC_{ant}-φC_T^0 and ΔC_{ant}-TTD are usually
591 less than 2 $\mu mol \cdot kg^{-1}$ meaning that there should be a good agreement between φC_T^0 and
592 TTD estimations of C_{ant} storages rates. The largest differences are found in the SAMW
593 layer and, mostly, in the AAIW layer. The SAMW in the EB (ΔC_{ant}-φC_T^0 rate < ΔC_{ant}-
594 TTD rate), where the OMZ is located, shows a decrease in O_2 concentration in 2010 (~3
595 $\mu mol \cdot kg^{-1}$). However, the AAIW layer displays an O_2 concentration decrease in 2010
596 (~8 $\mu mol \cdot kg^{-1}$) at the east of MAR, which parallels a slight increase in salinity (Brandt
597 et al., 2010), which has also been detected in our results (Table 2). The eastward
598 increase of salinity suggests a dilution of AAIW with surrounding water masses,
599 Mediterranean Water and, mainly, SACW, both of them with higher [C_{ant}] than AAIW.
600 It is also noticeable in our results that this AAIW layer at the eastern basin presents a
601 clear warming. This, together with the fact that Hernández-Guerra et al. (2014) found a
602 very strong decline in the AAIW northward transport, could be the reason why ΔC_{ant}-
603 φC_T^0 is higher than ΔC_{ant}-TTD in these layers. This will also have a large influence on
604 the C_{ant} storage rates (see section 3.4).

605 The objective of including the SS_ΔC_{ant} rates is to check whether C_{ant} has been
606 increasing at all depths along the section, in accordance to what is *expected* from a SS
607 accumulation of C_{ant}. The SS_ΔC_{ant} rates do not always match those obtained from the
608 bi-decadal ΔC_{ant} rates (Table 2). Since SS_ΔC_{ant} rates have to be interpreted as the
609 *expected* SS accumulation of C_{ant}, any *observed* (ΔC_{ant} rates) deviation from this could
610 be evidencing that the C_{ant} accumulation has been impacted by recent changes in
611 circulation or ventilation. Equally, when the ΔC_{ant} rates coincide with the SS_ΔC_{ant}
612 rates, it is an indication that the bi-decadal changes in C_{ant} follow a SS growing. When
613 comparing the ΔC_{ant}-φC_T^0 rates with the SS_ΔC_{ant}-φC_T^0 rates, there is no general pattern
614 throughout the water column. In the upper layers, the SACW ΔC_{ant}-φC_T^0 rates are lower
615 than the SS_ΔC_{ant}-φC_T^0 rates, while in the SAMW and AAIW the *observed* ΔC_{ant}-φC_T^0

rates are higher than the *expected* SS_ΔC_{ant}-φC_T^0 rates. In the deeper layers, most bi-decadal rates agree in their SS values, but there are some regions where the ΔC_{ant}-φC_T^0 rates show slightly lower values than the SS_ΔC_{ant}-φC_T^0 rates, as for example the uNADW in the EB region. When a comparison is made between the *observed* ΔC_{ant}-TTD and the *expected* SS_ΔC_{ant}-TTD rates, we find that most of the rates are comparable, with the exception of the SAMW in the EB region that displays much higher ΔC_{ant}-TTD rates than the SS_ΔC_{ant}-TTD rates. The reason why the ΔC_{ant}-TTD rates are so close to SS_ΔC_{ant}-TTD rates could be methodological, as the TTD method uses Inverse Gaussian functions (Waugh et al., 2004) that are based in the solution of an advection-diffusion equation with constant velocity and diffusivity, and a steady-steady circulation.

3.4 C_{ant} inventories

Table 3. Specific inventories of C_{ant}-ϕC_T^0 (iC_{ant}-ϕC_T^0) and Cant-TTD (iC_{ant}-TTD), in mol·m^{-2}, for each cruise and each region along 7.5°N. The shaded lines correspond to the 2010 inventories and the empty lines to the 1993 ones.

Year	iC_{ant}-ϕC_T^0 (mol·m^{-2})				iC_{ant}-TTD (mol·m^{-2})			
	WEST		EAST		WEST		EAST	
	WB	WR	ER	EB	WB	WR	ER	EB
1993	40.1±3.4	42.8±4.4	40.0±4.7	44.1±3.7	41.3±3.7	37.3±4.0	27.3±4.3	23.6±4.2
2010	56.1±3.5	62.2±4.0	58.2±4.5	56.7±4.0	57.4±3.7	53.3±4.2	37.0±4.3	32.9±4.1
1993	41.9±3.2		41.5±3.3		38.6±2.9		26.0±3.2	
2010	60.2±3.0		57.7±3.2		54.7±3.2		35.5±3.0	
1993	41.7±2.3				32.3±2.3			
2010	58.9±2.2				45.1±2.0			

Considering the complete 7.5°N section, we observe an increase of iC_{ant}-φC_T^0 from 41.7±2.3 mol·m^{-2} in 1993 to 58.9±2.2 mol·m^{-2} in 2010, and iC_{ant}-TTD from 32.3±2.3 mol·m^{-2} in 1993 to 45.1±2.0 mol·m^{-2} in 2010. The section averaged iC_{ant}-φC_T^0 values are higher than the iC_{ant}-TTD (Table 3), but both methods detect a similar increase in C_{ant} accumulation during the elapsed 17 years for the whole section: ~17 and ~13 mol·m^{-2}, for iC_{ant}-φC_T^0 and iC_{ant}-TTD, respectively. The differences are likely related to the assumptions behind each method and the different values in the waters below the 5ºC isotherm where, in general, the TTD method returns lower values (Vázquez-Rodríguez et al., 2009b). The TTD method is not expected to perfectly mimic C_{ant}-φC_T^0 because of the relatively recent introduction of tracers as CFCs (Tanhua et al., 2007).

Comparing the western and eastern basins, iC_{ant}-TTD values suggest a higher C_{ant} accumulation in the western than in the eastern basin in both cruises, while iC_{ant}-φC_T^0 shows similar values for both basins. To be precise, the WB is the region that displayed the highest iC_{ant}-TTD with a progressive decrease towards the EB region (Table 3). In 1993, the iC_{ant}-TTD was 38.6±2.9 mol·m^{-2} for the western basin and 26.0±3.2 mol·m^{-2} for the eastern basin. These results may be compared with the few related studies focused in the Equatorial Atlantic Ocean (Lee et al., 2003; Ríos et al., 2010; Steinfeldt et al., 2009; Vázquez-Rodríguez et al., 2009b). Our inventories (iC_{ant}-TTD) qualitatively agree with other studies that also support the idea of a greater accumulation of C_{ant} in the western basin compared to the eastern basin (Ríos et al., 2010; Vázquez-Rodríguez et al., 2009b). In the western basin, (Ríos et al., 2010) reported a C_{ant} specific inventory of ~38 mol·m^{-2} for the 7.5ºN latitude, based on a study using the TTD method in the WOCE A17N (1994) meridional transect. Their values are similar to our iC_{ant}-TTD (Table 3). In the eastern basin, an inventory of ~21 mol·m^{-2} was reported for the 7.5ºN latitude, from the CLIVAR A16N (2003) meridional transect (Vázquez-Rodríguez et al., 2009b), where the estimation of the C_{ant} inventory was obtained using the TTD method referred to the year 1994. Additionally, we may compare our iC_{ant}-TTD with the results from Steinfeldt et al. (2009) for the year 1997. These authors obtained values of 40-50 mol·m^{-2} in the western basin and 30-40 mol·m^{-2} in the eastern one, which are higher than our iC_{ant}-TTD, mostly because of the selected year of reference (1997 instead of 1993), but they reinforce our result of a higher C_{ant}-TTD accumulation at the western basin. Lee et al. (2003) reported contrasting results with respect to the east-west gradient in the C_{ant} inventories, between the Equator and 10ºN, using the ΔC^* method. They described a lower C_{ant} inventory in the West (~26.7 mol·m^{-2}) than in the East (~31.4 mol·m^{-2}) at these latitudes, taking as a reference the year 1994. The inventory reported by Lee et al. (2003) for the eastern basin is consistent with that reported by Vazquez-Rodríguez et al. (2009b). However, the underestimation of the western inventory by Lee et al. (2003) may be due to an unaccounted offset in the A_T data of the WOCE dataset, which was amended in the more recent work of Ríos et al. (2010).

3.5 C_{ant} storage rates

Table 4. C_{ant} and SS_C_{ant} rates (mol·m^{-2}·y^{-1}) for the western and eastern basins and for the whole 7.5°N section, as obtained using the ϕC_T^0 and TTD methods. The C_{ant} and SS_C_{ant} storage rates are also shown for the upper (regular font) and lower layers (grey italics) defined in the western and eastern basins.

C_{ant} storage rate (mol·m^{-2}·y^{-1})	Western basin		Eastern basin		7.5°N
	All	Upper/*Lower*	All	Upper/*Lower*	All
C_{ant}-ϕC_T^0	1.07±0.23	0.67±0.07 / *0.40±0.21*	0.95±0.27	0.76±0.08 / *0.19±0.26*	1.01±0.18
SS_C_{ant}-ϕC_T^0	0.86±0.04	0.41±0.01 / *0.45±0.04*	0.84±0.04	0.41±0.01 / *0.43±0.04*	0.85±0.03
C_{ant}-TTD	0.95±0.24	0.44±0.09 / *0.50±0.22*	0.56±0.25	0.46±0.08 / *0.10±0.24*	0.75±0.17
SS_C_{ant}-TTD	0.79±0.04	0.36±0.01 / *0.42±0.04*	0.52±0.04	0.33±0.01 / *0.19±0.04*	0.65±0.03

In order to provide an overall view of the C_{ant} accumulation for the 7.5ºN transect, the iC_{ant}-φC_T^0 storage rate was calculated for the whole section, obtaining a value of 1.01±0.18 mol·m^{-2}·y^{-1}, which is higher than the C_{ant}-TTD storage rate (0.75±0.17 mol·m^{-2}·y^{-1}) (Table 4). The East and West components of the C_{ant} storage rates reveal that both basins have been accumulating C_{ant}-φC_T^0 at approximately the same rate (1.07±0.23 and 0.95±0.27 mol·m^{-2}·y^{-1}, in the western and eastern basins, respectively). However, the C_{ant}-TTD storage rates suggest a relatively faster rate of accumulation in the WB (0.95±0.24 mol·m^{-2}·y^{-1}) than the EB (0.56±0.25 mol·m^{-2}·y^{-1}).

In addition, by dividing the water column into two layers, we considered separately the rate of increase occurring in the upper and the deeper water masses of the section: an "*upper layer*" enclosing the SACW, SAMW and AAIW layers, and a "*lower layer*" enclosing the uNADW, lNADW and AABW layers. These two partitions were also divided into their respective western and eastern basins. Within the uncertainties, both the C_{ant}-φC_T^0 and C_{ant}-TTD storage rates show similar values in the *upper layer* at the western and eastern basins together, slightly larger than those found in the *lower layer* (Table 4). The important role of the NADW in the C_{ant} storage suggested by Steinfeldt et al. (2009) is emphasized by both methods, showing a faster C_{ant} increase in the western *lower layer* than in the eastern one (Table 4).

The *observed* C_{ant} storage rates (Table 4) are slightly higher than the *expected* SS_C_{ant}-φC_T^0 (0.85±0.03 mol·m^{-2}·y^{-1}) and SS_C_{ant}-TTD (0.65±0.03 mol·m^{-2}·y^{-1}) rates found in the 7.5°N section, but both are consistent if the uncertainties are considered. These

results suggest that the mean [C_{ant}] over the whole section has been increasing at a similar pace as *expected* assuming SS. Regarding the SS_C_{ant}-φC_T^0 rates, these suggest that the growth in both basins has been quite similar (Table 4), while the SS_C_{ant}-TTD rates propose a slower growth in the eastern basin, which agrees with the C_{ant}-TTD storage rate value found for that basin. Overall, the SS_C_{ant}-φC_T^0 rates suggest a C_{ant} increase with time of around 0.4 $mol \cdot m^{-2} \cdot y^{-1}$ for each layer and basin. The SS_C_{ant}-TTD rates suggest a similar rate in the *upper layer* of both basins (~0.3 $mol \cdot m^{-2} \cdot y^{-1}$), while in the *lower layer*, those rates exhibit a slower growth at the eastern basin (Table 4). We find that the *upper layer* in the western basin shows C_{ant}-TTD rates very close but higher than the SS_C_{ant}-TTD storage rate. This could be mostly influenced by the SAMW layer, which displays a ΔC_{ant}-TTD rate much higher than SS_ΔC_{ant}-TTD rates (Table 2). The C_{ant}-φC_T^0 storage rate shows a higher rate than SS_C_{ant}-φC_T^0 rate (Table 4). For this method, the most influent layers are the SAMW and AAIW, which show larger ΔC_{ant}-φC_T^0 rates than SS_ΔC_{ant}-φC_T^0 rates (Table 2). In the western *lower layer*, both the *observed* C_{ant}-φC_T^0 and C_{ant}-TTD storage rates agree with their *expected* SS_C_{ant}-φC_T^0 and SS_C_{ant}-TTD rates (Table 4), indicating that the western *lower layer* is accumulating C_{ant} at a steady state pace, independently of the method used, in agreement with the previous description of SS_ΔC_{ant}-TTD and ΔC_{ant}-TTD rates (Table 2).

Regarding the eastern basin, the *upper layer* experienced C_{ant} storage rates higher than SS_C_{ant} rates. As we previously detected in the C_{ant} distribution and their changes (Table 2), the SAMW and AAIW show again the largest mismatch in the *upper layer*, showing a higher C_{ant}-φC_T^0 storage rate than SS_C_{ant}-φC_T^0 rate (Table 4). This could be directly related to the decrease in the AMOC between 1993 and 2010 induced by the retreat of the AAIW (San Antolín Plaza et al., 2012; Hernández-Guerra et al., 2014), as suggested by the changes in salinity (Table 2). On the other hand, the *observed* C_{ant}-TTD storage rates are slightly higher but agree with the *expected* SS rates. In the eastern *lower layer*, the *observed* C_{ant}-TTD storage rate reflects the *expected* SS_C_{ant}-TTD rates, which also match the C_{ant}-φC_T^0 storage rate. Hence, we suggest that the C_{ant} in the eastern *lower layer* is growing at steady state pace. However, the SS_C_{ant}-φC_T^0 rate is higher than the C_{ant}-φC_T^0 rate, which could be due to the larger SS_ΔC_{ant}-φC_T^0 rates found in the EB for the uNADW and lNADW (Table 2). As suggested before, the decrease in the AMOC affecting the uNADW (Hernández-Guerra et al., 2014) and the

729 dilution of the C_{ant} signal with the less C_{ant}-loaded surrounding waters could influence
730 these results.

731 To sum up, when comparing the *observed* C_{ant} storage rates with the *expected* SS_C_{ant}
732 rates (for both the φC_T^0 and TTD methods), our results suggest that C_{ant} has been
733 accumulating at a steady state rate in the *lower layer*, while the rates for the *upper layer*
734 exhibit a faster growing, mostly influenced by the weakening of the northward flow of
735 AAIW. Despite the faster rates in the *upper layer*, the *lower layer* presents higher
736 uncertainty in its values. This relatively large error of the C_{ant} storage rates for the lower
737 layer makes it impossible to detect a [C_{ant}] increase that is significantly different from
738 the steady state assumption.

739 4. Conclusions

740 The distribution of anthropogenic CO_2 (C_{ant}) along the 7.5ºN section in 2010, as
741 estimated by the φC_T^0 and TTD methods, reveals higher values and a deeper penetration
742 of the anthropogenic signal in the South Atlantic Central Water layer with respect to the
743 distribution found in 1993, while the C_{ant} core in the Antarctic Intermediate Water layer
744 is narrower in 2010 than in 1993. In the deep layers, the signal of the Labrador Sea
745 Water within the upper North Atlantic Deep Water layer (uNADW) is clear, having a
746 stronger presence in the eastern basins of the section in 2010. The difference in the C_{ant}
747 signal of the uNADW between 1993 and 2010 in the region adjacent to the West of the
748 Mid-Atlantic Ridge leads to a ΔC_{ant}-φC_T^0 rate as high as 0.18±0.03 $\mu mol \cdot kg^{-1} \cdot y^{-1}$, in
749 agreement with the ΔC_{ant}-TTD rate of 0.17±0.03 $\mu mol \cdot kg^{-1} \cdot y^{-1}$.

750 The C_{ant}-φC_T^0 specific inventories (iC_T^0-C_{ant}) found for the whole section are 41.7±2.3
751 $mol \cdot m^{-2}$ in 1993 and 58.9±2.2 $mol \cdot m^{-2}$ in 2010, while the C_{ant}-TTD specific inventories
752 (iC_{ant}-TTD) are lower: 32.3±2.3 $mol \cdot m^{-2}$ in 1993 and 45.1±2.0 $mol \cdot m^{-2}$ in 2010. For
753 both cruises, the iC_{ant}-TTD is higher in the western basin than in the eastern basin. The
754 C_{ant}-φC_T^0 storage rate for the whole section over the studied period is 1.01±0.18 $mol \cdot m^{-2} \cdot y^{-1}$,
755 slightly higher but in agreement, within the uncertainties, with the C_{ant}-TTD
756 storage rate of 0.75±0.17 $mol \cdot m^{-2} \cdot y^{-1}$. When compared with the expected SS_C_{ant} rates,
757 these observed C_{ant} storage rates suggest that C_{ant} was accumulating close to a steady
758 state rate. When dividing the water column at a depth of ~1000 m, the C_{ant} of the lower
759 layer generally grows at steady state pace, while the upper layer increases faster. This is

760 mainly due to a weakening of the northward advection of the Antarctic Intermediate
761 Water, with the influence of the more C_{ant}-loaded surrounding waters favouring the C_{ant}
762 increase.

763 Acknowledgments

764 Thanks are due to the cruise participants of the MOC2 cruise, the BIO Hespérides crew
765 and the scientific and technical team, for their indispensable help. We also wish to thank
766 A. Velo for his support with the 3DwMLR method, Paula C. Pardo for her very useful
767 comments and advices and two anonymous reviewers for their careful reading and their
768 many insightful and constructive comments This work was funded by the 7th
769 Framework Programme (EU FP7 CARBOCHANGE, under grand agreement no.
770 264879) and by the Spanish Ministry of Economy and Competitiveness through
771 Projects GHGMOC (CTM2009-07574-E), MOC2 (CTM2008-06438-C02-01/MAR)
772 and ESCLAT (CTM2009-07405-E/MAR) and by the Deutsche
773 Forschungsgemeinschaft (DFG) (M. Rhein, grant Rh25/36-1). FFP and AFR were
774 supported by the Spanish Government and co-founded by the European Regional
775 Development Fund (CTM2013-41048-P).

776 References

777 Álvarez, M., Ríos, A.F., Pérez, F.F., Bryden, H.L., Rosón, G., 2003. Transports and
778 budgets of total inorganic carbon in the subpolar and temperate North Atlantic.
779 Glob. Biogeochem Cycles 17, 1002. doi:10.1029/2002GB001881
780 Andrié, C., Ternon, J.-F., Messias, M.-J., Memery, L., Bourlès, B., 1998.
781 Chlorofluoromethane distributions in the deep equatorial Atlantic during
782 January–March 1993. Deep Sea Res. Part Oceanogr. Res. Pap. 45, 903–930.
783 doi:10.1016/S0967-0637(98)00003-X
784 Arhan, M., Mercier, H., Bourles, B., Gouriou, Y., 1998. Hydrographic sections across
785 the Atlantic at 7º30N and 4º30S. Deep Sea Res. Part Oceanogr. Res. Pap. 45,
786 829–872.
787 Ballantyne, A.P., Alden, C.B., Miller, J.B., Tans, P.P., White, J.W.C., 2012. Increase in
788 observed net carbon dioxide uptake by land and oceans during the past 50 years.
789 Nature 488, 70–72.
790 Brandt, P., Greatbatch, R.J., Claus, M., Didwischus, S.-H., Hormann, V., Funk, A.,
791 Hahn, J., Krahmann, G., Fischer, J., Körtzinger, A., 2012. Ventilation of the
792 equatorial Atlantic by the equatorial deep jets. J. Geophys. Res. Oceans 117,
793 C12015. doi:10.1029/2012JC008118
794 Brandt, P., Hormann, V., Körtzinger, A., Visbeck, M., Krahmann, G., Stramma, L.,
795 Lumpkin, R., Schmid, C., 2010. Changes in the ventilation of the oxygen
796 minimum zone of the tropical North Atlantic. J. Phys. Oceanogr. 40, 1784–1801.
797 doi:10.1175/2010JPO4301.1

798 Brea, S., Álvarez-Salgado, X.A., Álvarez, M., Pérez, F.F., Mémery, L., Mercier, H.,
799 Messias, M.J., 2004. Nutrient mineralization rates and ratios in the eastern South
800 Atlantic. J. Geophys. Res. 109. doi:10.1029/2003JC002051
801 Brewer, P.G., 1978. Direct observation of the oceanic CO_2 increase. Geophys. Res. Lett.
802 5, 997–1000. doi:10.1029/GL005i012p00997
803 Bulsiewicz, K., Rose, H., Klatt, O., Putzka, A., Roether, W., 1998. A capillary-column
804 chromatographic system for efficient chlorofluorocarbon measurement in ocean
805 waters. J. Geophys. Res. Oceans 1978–2012 103, 15959–15970.
806 Ciais, P., Sabine, C., Bala, G. , Bopp, L., Brovkin, V., Canadell, J. , Chhabra, A.,
807 DeFries, R., Galloway, J., Heimann, M., Jones, C., Le Quéré, C., Myneni, R.B.,
808 Piao, S., Thornton, P., 2013: Carbon and Other Biogeochemical Cycles. In:
809 Climate Change 2013: The Physical Science Basis. Contribution of Working
810 Group I to the Fifth Assessment Report of the Intergovernmental Panel on
811 Climate Change [Stocker, T.F., D. Qin, G.-K. Plattner, M. Tignor, S.K. Allen, J.
812 Boschung, A. Nauels, Y. Xia, V. Bex and P.M. Midgley (eds.)]. Cambridge
813 University Press, Cambridge, United Kingdom and New York, NY, USA.
814 Chen, G.-T., Millero, F.J., 1979. Gradual increase of oceanic CO_2. Nature 277, 205–
815 206. doi:10.1038/277205a0
816 Clayton, T.D., Byrne, R.H., 1993. Spectrophotometric seawater pH measurements: total
817 hydrogen ion concentration scale calibration of m-cresol purple and at-sea
818 results. Deep-Sea Res. 40, 2115–2129.
819 Culberson, C.H., 1991. WOCE operations manual (WHP operations and methods),
820 WHPO 91/1. Woods Hole Oceanogr. Inst., Woods Hole, Mass.
821 DelValls, T., Dickson, A., 1998. The pH of buffers based on 2-amino-2-hydroxymethyl-
822 1, 3-propanediol (“tris”) in synthetic sea water. Deep-Sea Res. Part I 45, 1541–
823 1554.
824 Dickson, A., Millero, F., 1987. A comparison of the equilibrium constants for the
825 dissociation of carbonic acid in seawater media. Deep-Sea Res. 34, 1733–1743.
826 doi:10.1016/0198-0149(87)90021-5
827 Friis, K., Körtzinger, A., Pätsch, J., Wallace, D.W.R., 2005. On the temporal increase of
828 anthropogenic CO_2 in the subpolar North Atlantic. Deep Sea Res. Part
829 Oceanogr. Res. Pap. 52, 681–698. doi:10.1016/j.dsr.2004.11.017
830 Gammon, R.H., Cline, J., Wisegarver, D., 1982. Chlorofluoromethanes in the northeast
831 Pacific Ocean: Measured vertical distributions and application as transient
832 tracers of upper ocean mixing. J. Geophys. Res. Oceans 1978–2012 87, 9441–
833 9454.
834 Gieskes, J.M., 1969. Effect of temperature on the pH of seawater. Limnol. Oceanogr.
835 14, 679–685. doi:10.4319/lo.1969.14.5.0679
836 Gouretski, V.V., Jancke, K., 2000. Systematic errors as the cause for an apparent deep
837 water property variability: global analysis of the WOCE and historical
838 hydrographic data. Prog. Oceanogr. 48, 337–402.
839 doi:http://dx.doi.org/10.1016/S0079-6611(00)00049-5
840 Gruber, N., Gloor, M., Mikaloff Fletcher, S.E., Doney, S.C., Dutkiewicz, S., Follows,
841 M.J., Gerber, M., Jacobson, A.R., Joos, F., Lindsay, K., Menemenlis, D.,
842 Mouchet, A., Müller, S.A., Sarmiento, J.L., Takahashi, T., 2009. Oceanic
843 sources, sinks, and transport of atmospheric CO_2. Glob. Biogeochem. Cycles 23.
844 doi:10.1029/2008GB003349
845 Gruber, N., Sarmiento, J.L., Stocker, T.F., 1996. An improved method for detecting
846 anthropogenic CO_2 in the oceans. Glob. Biogeochem. Cycles 10, 809–837.

Guallart, E.F., Schuster, U., Fajar, N.M., Legge, O., Brown, P., Pelejero, C., Messias, M.-J., Calvo, E., Watson, A., Ríos, A.F., Pérez, F.F., 2014. Trends in anthropogenic CO_2 in water masses of the Subtropical North Atlantic Ocean. Prog. Oceanogr. doi:10.1016/j.pocean.2014.11.006

Hernández-Guerra, A., Pelegrí, J.L., Fraile-Nuez, E., Benítez-Barrios, V., Emelianov, M., Pérez-Hernández, M.D., Vélez-Belchí, P., 2014. Meridional overturning transports at 7.5N and 24.5N in the Atlantic Ocean during 1992–93 and 2010–11. Prog. Oceanogr. 128, 98–114. doi:10.1016/j.pocean.2014.08.016

Herraiz-Borreguero, L., Rintoul, S.R., 2011. Subantarctic mode water: distribution and circulation. Ocean Dyn. 61, 103–126. doi:10.1007/s10236-010-0352-9

Holfort, J., Johnson, K.M., Schneider, B., Siedler, G., Wallace, D.W., 1998. Meridional transport of dissolved inorganic carbon in the South Atlantic Ocean. Glob. Biogeochem. Cycles 12, 479–499.

Johnson, G.C., 2008. Quantifying Antarctic bottom water and North Atlantic deep water volumes. J Geophys Res 113, C05027. doi:10.1029/2007JC004477

Johnson, K.M., Wills, K.D., Butler, D.B., Johnson, W.K., Wong, C.S., 1993. Coulometric total carbon dioxide analysis for marine studies: maximizing the performance of an automated gas extraction system and coulometric detector. Mar. Chem. 44, 167–187.

Keeling, C.D., Bolin, B., 1967. The simultaneous use of chemical tracers in oceanic studies I. General theory of reservoir models. Tellus 19, 566–581. doi:10.1111/j.2153-3490.1967.tb01509.x

Key, R.M., Tanhua, T., Olsen, A., Hoppema, M., Jutterström, S., Schirnick, C., van Heuven, S., Kozyr, A., Lin, X., Velo, A., Wallace, D.W.R., Mintrop, L., 2010. The CARINA data synthesis project: Introduction and overview. Earth Syst Sci Data 2, 105–121. doi:10.5194/essd-2-105-2010

Khatiwala, S., Primeau, F., Hall, T., 2009. Reconstruction of the history of anthropogenic CO2 concentrations in the ocean, Nature, 462, 346–349, doi:10.1038/nature08526.

Khatiwala, S., Tanhua, T., Mikaloff Fletcher, S., Gerber, M., Doney, S.C., Graven, H.D., Gruber, N., McKinley, G.A., Murata, A., Ríos, A.F., Sabine, C.L., 2013. Global ocean storage of anthropogenic carbon. Biogeosciences 10, 2169–2191. doi:10.5194/bg-10-2169-2013

Lazier, J., Hendry, R., Clarke, A., Yashayaev, I., Rhines, P., 2002. Convection and restratification in the Labrador Sea, 1990–2000. Deep Sea Res. Part Oceanogr. Res. Pap. 49, 1819–1835. doi:10.1016/S0967-0637(02)00064-X

Lee, K., Choi, S.D., Park, G.H., Wanninkhof, R., Peng, T.H., Key, R.M., Sabine, C.L., Feely, R.A., Bullister, J.L., Millero, F.J., 2003. An updated anthropogenic CO_2 inventory in the Atlantic Ocean. Glob. Biogeochem. Cycles 17, 1116. doi:10.1029/2003GB002067

Le Quéré, C., Andres, R.J., Boden, T., Conway, T., Houghton, R.A., House, J.I., Marland, G., Peters, G.P., van der Werf, G.R., Ahlström, A., Andrew, R. M., Bopp, L., Canadell, J. G., Ciais, P., Doney, S. C., Enright, C., Friedlingstein, P., Huntingford, C., Jain, A. K., Jourdain, C., Kato, E., Keeling, R. F., Klein Goldewijk, K., Levis, S., Levy, P., Lomas, M., Poulter, B., Raupach, M. R., Schwinger, J., Sitch, S., Stocker, B. D., Viovy, N., Zaehle, S., and Zeng, N., 2013. The global carbon budget 1959-2011. Earth Syst. Sci. Data 5, 165–185. doi:10.5194/essd-5-165-2013

Le Quéré, C., Moriarty, R., Andrew, R.M., Peters, G.P., Ciais, P., Friedlingstein, P., Jones, S.D., Sitch, S., Tans, P., Arneth, A., Boden, T.A., Bopp, L., Bozec, Y.,

Canadell, J.G., Chevallier, F., Cosca, C.E., Harris, I., Hoppema, M., Houghton, R.A., House, J.I., Jain, A., Johannessen, T., Kato, E., Keeling, R.F., Kitidis, V., Klein Goldewijk, K., Koven, C., Landa, C.S., Landschützer, P., Lenton, A., Lima, I.D., Marland, G., Mathis, J.T., Metzl, N., Nojiri, Y., Olsen, A., Ono, T., Peters, W., Pfeil, B., Poulter, B., Raupach, M.R., Regnier, P., Rödenbeck, C., Saito, S., Salisbury, J.E., Schuster, U., Schwinger, J., Séférian, R., Segschneider, J., Steinhoff, T., Stocker, B.D., Sutton, A.J., Takahashi, T., Tilbrook, B., van der Werf, G.R., Viovy, N., Wang, Y.-P., Wanninkhof, R., Wiltshire, A., Zeng, N., 2014. Global carbon budget 2014. Earth Syst Sci Data Discuss 7, 521–610. doi:10.5194/essdd-7-521-2014

Le Quéré, C., Raupach, M.R., Canadell, J.G., Marland, G., Bopp, L., Conway, T.J., Doney, S.C., Feely, R.A., Foster, P., Friedlingstein, P., Gurney, K., Houghton, R.A., House, J.I., Huntingford, C., Levy, P.E., Lomas, M.R., Majkut, J., Metzl, N., Ometto, J.P., Peters, G.., Prentice, I.C., Randerson, J.T., Running, S.W., Sarmiento, J.L., Schuster, U., Sitch, S., Takahashi, T., Viovy, N., van der Werf, G.R., Woodward, F.I., 2009. Trends in the sources and sinks of carbon dioxide. Nat. Geosci. 2, 831–836. doi:10.1038/ngeo689

Lo Monaco, C., Goyet, C., Metzl, N., Poisson, A., Touratier, F., 2005. Distribution and inventory of anthropogenic CO_2 in the Southern Ocean: Comparison of three data-based methods. J Geophys Res 110, 9. doi:10.1029/2004JC002571

Mehrbach, C., Culberson, C., Hawley, J., Pytkowicz, R., 1973. Measurement of the apparent dissociation constants of carbonic acid in seawater at atmospheric pressure. Limnol. Oceanogr. 897–907.

Mémery, L., Arhan, M., Álvarez-Salgado, X.A., Messias, M.J., Mercier, H., Castro, C.G., Ríos, A.F., 2000. The water masses along the western boundary of the south and equatorial Atlantic. Prog. Oceanogr. 47, 69–98. doi:10.1016/S0079-6611(00)00032-X

Mikaloff Fletcher, S.E., Gruber, N., Jacobson, A.R., Doney, S.C., Dutkiewicz, S., Gerber, M., Follows, M., Joos, F., Lindsay, K., Menemenlis, D., others, 2006. Inverse estimates of anthropogenic CO_2 uptake, transport, and storage by the ocean. Glob. Biogeochem. Cycles 20. doi:10.1029/2005GB002530

Millero, F.J., 1979. The thermodynamics of the carbonate system in seawater. Geochim. Cosmochim. Acta 43, 1651–1661. doi:10.1016/0016-7037(79)90184-4

Mintrop, L., Pérez, F., González-Dávila, M., Santana-Casiano, J., Körtzinger, A., 2000. Alkalinity determination by potentiometry: Intercalibration using three different methods. Cienc. Mar. 26, 23–37.

Murata, A., Kumamoto, Y., Sasaki, K., Watanabe, S., Fukasawa, M., 2008. Decadal increases of anthropogenic CO_2 in the subtropical South Atlantic Ocean along 30 S. J Geophys Res 113, C06007. doi:10.1029/2007JC004424

Oudot, C., 1993. Total CO_2 and Total Alkalinity Data Obtained during the R/V L'Atalante cruise in the Atlantic Ocean (WOCE Section A06, 02 Jan. - 10 Feb., 1993). Carbon Dioxide Information Analysis Center, Oak Ridge National Laboratory, US Department of Energy, Oak Ridge, Tennessee. doi:10.3334/CDIAC/otg.WOCE_A06_1993

Oudot, C., Morin, P., Baurand, F., Wafar, M., Corre, P.L., 1998. Northern and southern water masses in the equatorial Atlantic distribution of nutrients on the WOCE A6 and A7 lines. Deep-Sea Res. Part I 45, 873–902. doi:10.1016/S0967-0637(98)00002-8

945 Oudot, C., Ternon, J.F., 1994. Mesures des paramètres du système CO_2 Recueil de
946 Données, Campagne CITHER 1, (Traceurs géochimiques/2). Doc Sci
947 0ORSTOM Cayenne 4, 9–48.
948 Oudot, C., Ternon, J.F., Lecomte, J., 1995. Measurements of atmospheric and oceanic
949 CO_2 in the tropical Atlantic: 10 years after the 1982-1984 FOCAL cruises.
950 Tellus B 47, 70–85. doi:10.1034/j.1600-0889.47.issue1.8.x
951 Pérez, F.F., Fraga, F., 1987. A precise and rapid analytical procedure for alkalinity
952 determination. Mar. Chem. 21, 169–182. doi:10.1016/0304-4203(87)90037-5
953 Pérez, F.F., Mercier, H., Vázquez-Rodríguez, M., Lherminier, P., Velo, A., Pardo, P.C.,
954 Rosón, G., Ríos, A.F., 2013. Atlantic Ocean CO_2 uptake reduced by weakening
955 of the meridional overturning circulation. Nat. Geosci. 6, 146–152.
956 doi:10.1038/ngeo1680.
957 Plancherel, Y., Rodgers, K. B., Key, R.M., Jacobson, A. R., Sarmiento, J.L., 2013 Role
958 of regression model selection and station distribution on the estimation of
959 oceanic anthropogenic carbon change by eMLR, Biogeosciences, 10, 4801-
960 4831, doi:10.5194/bg-10-4801-2013
961 Rhein, M., Stramma, L., Krahmann, G., 1998. The spreading of Antarctic Bottom Water
962 in the tropical Atlantic. Deep Sea Res.-Part -Oceanogr. Res. Pap. 45, 507–528.
963 doi:10.1016/S0967-0637(97)00030-7
964 Ríos, A.F., Pérez, F.F., Pelegrí, J.L., Fajar, N.M., 2012a. Carbon Data Obtained During
965 the R/V Hesperides Cruise in the Atlantic Ocean on CLIVAR Repeat
966 Hydrography Section A06 (5 April - 16 May, 2010). Carbon Dioxide
967 Information Analysis Center, Oak Ridge National Laboratory, US Department
968 of Energy, Oak Ridge, Tennessee.
969 doi:10.3334/CDIAC/OTG.CLIVAR_A06_2010
970 Ríos, A.F., Vázquez-Rodríguez, M., Padín, X.A., Pérez, F.F., 2010. Anthropogenic
971 carbon dioxide in the South Atlantic western basin. J. Mar. Syst. 83, 38–44.
972 doi:http://dx.doi.org/10.1016/j.jmarsys.2010.06.010
973 Ríos, A.F., Velo, A., Pardo, P.C., Hoppema, M., Pérez, F.F., 2012b. An update of
974 anthropogenic CO_2 storage rates in the western South Atlantic basin and the role
975 of Antarctic Bottom Water. J. Mar. Syst. 94, 197–203.
976 doi:10.1016/j.jmarsys.2011.11.023
977 Rosell-Fieschi, M., Pelegrí, J.L., Gourrion, J., 2014. Zonal jets in the equatorial Atlantic
978 Ocean. Prog. Oceanogr.130, 1-18. doi:10.1016/j.pocean.2014.08.008
979 Roson, G., Rios, A.F., Perez, F. F., Lavin, A., Bryden, H. L., 2003. Carbon distribution,
980 fluxes, and budgets in the subtropical North Atlantic Ocean (24.5º N), J.
981 Geophys. Res., 108(C5), 3144, doi:10.1029/1999JC000047.
982 Sabine, C.L., Feely, R.A., Gruber, N., Key, R.M., Lee, K., Bullister, J.L., Wanninkhof,
983 R., Wong, C.S., Wallace, D.W.R., Tilbrook, B., Millero, F.J., Peng, T.-H.,
984 Kozyr, A., Ono, T., Rios, A.F., 2004. The Oceanic Sink for Anthropogenic CO_2.
985 Science 305, 367–371. doi:10.1126/science.1097403
986 San Antolín Plaza, M.Á., Pelegrí, J.L., Machín, F.J., Benítez Barrios, V., 2012. Inter-
987 decadal changes in stratification and double diffusion in a transatlantic section
988 along 7.5 N. Sci. Mar. 76, 189–207. doi:10.3989/scimar.03616.19G
989 Sarafanov, A., Sokov, A., Demidov, A., 2007. Water mass characteristics in the
990 equatorial North Atlantic: A section nominally along 6.5°N, July 2000. J.
991 Geophys. Res. Oceans 112, C12023. doi:10.1029/2007JC004222
992 Steinfeldt, R., Rhein, M., Bullister, J.L., Tanhua, T., 2009. Inventory changes in
993 anthropogenic carbon from 1997-2003 in the Atlantic Ocean between 20°S and
994 65°N. Glob. Biogeochem. Cycles 23, GB3010. doi:10.1029/2008GB003311

995 Steinfeldt, R., Rhein, M., Walter, M., 2007. NADW transformation at the western
996 boundary between 66W/20N and 60W/10N. Deep Sea Res. Part Oceanogr. Res.
997 Pap. 54, 835–855. doi:10.1016/j.dsr.2007.03.004
998 Stramma, L., Brandt, P., Schafstall, J., Schott, F., Fischer, J., Körtzinger, A., 2008.
999 Oxygen minimum zone in the North Atlantic south and east of the Cape Verde
1000 Islands. J Geophys Res 113.
1001 Stramma, L., England, M., 1999. On the water masses and mean circulation of the
1002 South Atlantic Ocean. J. Geophys. Res. 104, 20863–20.
1003 doi:10.1029/1999JC900139
1004 Stramma, L., Schott, F., 1999. The mean flow field of the tropical Atlantic Ocean. Deep
1005 Sea Res.-Part II-Top. Stud. Oceanogr. 46, 279–304. doi:10.1016/S0967-
1006 0645(98)00109-X
1007 Tanhua, T., Biastoch, A., Körtzinger, A., Lüger, H., Böning, C., Wallace, D.W.R.,
1008 2006. Changes of anthropogenic CO_2 and CFCs in the North Atlantic between
1009 1981 and 2004. Glob. Biogeochem. Cycles 20, GB4017.
1010 doi:10.1029/2006GB002695
1011 Tanhua, T., Körtzinger, A., Friis, K., Waugh, D.W., Wallace, D.W.., 2007. An estimate
1012 of anthropogenic CO_2 inventory from decadal changes in oceanic carbon
1013 content. Proc. Natl. Acad. Sci. 104, 3037. doi:10.1073/pnas.0606574104
1014 Tanhua, T., van Heuven, S., Key, R.M., Velo, A., Olsen, A., Schirnick, C., 2010.
1015 Quality control procedures and methods of the CARINA database. Earth Syst
1016 Sci Data 2, 35–49. doi:10.5194/essd-2-35-2010, 2010
1017 Tans, P., Keeling, R., 2014. Trends in Atmospheric Carbon Dioxide [WWW
1018 Document]. URL http://www.esrl.noaa.gov/gmd/ccgg/trends/
1019 Ternon, J.F., Oudot, C., Gourlaouen, V., Diverres, D., 2001. The determination of pHT
1020 in the equatorial Atlantic Ocean and its role in the sound absorption modeling in
1021 seawater. J. Mar. Syst. 30, 67–87. doi:10.1016/S0924-7963(01)00038-0
1022 Thomas, H., Ittekkot, V., 2001. Determination of anthropogenic CO_2 in the North
1023 Atlantic Ocean using water mass ages and CO_2 equilibrium chemistry. J. Mar.
1024 Syst. 27, 325–336. doi:10.1016/S0924-7963(00)00077-4
1025 Touratier, F., Azouzi, L., Goyet, C., 2007. CFC-11, D14C and 3H tracers as a means to
1026 assess anthropogenic CO_2 concentrations in the ocean. Tellus B 59, 318–325.
1027 doi:10.1111/j.1600-0889.2006.00247.x
1028 Tsuchiya, M., Talley, L.D., McCartney, M.S., 1994. Water-mass distributions in the
1029 western South Atlantic; A section from South Georgia Island (54S) northward
1030 across the equator. J. Mar. Res. 52, 55–81.
1031 doi:http://dx.doi.org/10.1357/0022240943076759
1032 Urbano, D.F., De Almeida, R.A.F., Nobre, P., Hay, A.E., Williams, G.D., Bindoff,
1033 N.L., Marsland, S.J., Rintoul, S.R., Anderson, C.R., Siegel, D.A., 2008.
1034 Equatorial Undercurrent and North Equatorial Countercurrent at 38 W: A new
1035 perspective from direct velocity data. J Geophys Res 113, C04041.
1036 Van Heuven, S.M.A.C., Hoppema, M., Huhn, O., Slagter, H.A., de Baar, H.J.W., 2011.
1037 Direct observation of increasing CO_2 in the Weddell Gyre along the Prime
1038 Meridian during 1973–2008. Deep Sea Res. Part II Top. Stud. Oceanogr.,
1039 Physics, Carbon Dioxide, Trace Elements and Isotopes in the Southern Ocean:
1040 The Polarstern Expeditions ANT XXIV-3 (2008) and ANT XXIII/3 (2006) 58,
1041 2613–2635. doi:10.1016/j.dsr2.2011.08.007
1042 Van Heuven, S., Pierrot, D., Lewis, E., Wallace, D., 2009. MATLAB Program
1043 developed for CO_2 system calculations. ORNL/CDIAC-105b, Carbon Dioxide

Information Analysis Center, Oak Ridge National Laboratory, U.S. Department of Energy, Oak Ridge, Tennessee.

Vázquez-Rodríguez, M., Padin, X.A., Pardo, P.C., Ríos, A.F., Pérez, F.F., 2012. The subsurface layer reference to calculate preformed alkalinity and air–sea CO_2 disequilibrium in the Atlantic Ocean. J. Mar. Syst. 94, 52–63. doi:10.1016/j.jmarsys.2011.10.008

Vázquez-Rodríguez, M., Padín, X.A., Ríos, A.F., Bellerby, R.G.J., Pérez, F.F., 2009a. An upgraded carbon-based method to estimate the anthropogenic fraction of dissolved CO_2 in the Atlantic Ocean. Biogeosciences Discuss 6, 4527–4571. doi:10.1016/j.jmarsys.2011.11.023

Vázquez-Rodríguez, M., Touratier, F., Lo Monaco, C., Waugh, D.W., Padin, X.A., Bellerby, R.G.J., Goyet, C., Metzl, N., Ríos, A.F., Pérez, F.F., 2009b. Anthropogenic carbon distributions in the Atlantic Ocean: data-based estimates from the Arctic to the Antarctic. Biogeosciences 6, 439–451. doi:10.5194/bg-6-439-2009

Velo, A., Pérez, F.F., Tanhua, T., Gilcoto, M., Ríos, A.F., Key, R.M., 2013. Total alkalinity estimation using MLR and neural network techniques. J. Mar. Syst. 111–112, 11–18. doi:10.1016/j.jmarsys.2012.09.002

Walker, S.J., Weiss, R.F., Salameh, P.K., 2000. Reconstructed histories of the annual mean atmospheric mole fractions for the halocarbons CFC-11 CFC-12, CFC-113, and carbon tetrachloride. J. Geophys. Res. Oceans 1978–2012 105, 14285–14296.

Wanninkhof, R., Doney, S.C., Bullister, J.L., Levine, N.M., Warner, M., Gruber, N., 2010. Detecting anthropogenic CO_2 changes in the interior Atlantic Ocean between 1989 and 2005. J. Geophys. Res. Oceans 115, C11028. doi:10.1029/2010JC006251

Wanninkhof, R., Tsung-Hung, P., Huss, B., Sabine, C.L., Lee, K., 2003. Comparison of inorganic carbon system parameters measured in the Atlantic Ocean from 1990 to 1998 and recommended adjustments. Carbon Dioxide Information Analysis Center, Oak Ridge National Laboratory, ORNL/CDIAC-140. doi:10.2172/814517

Warner, M.J., Weiss, R.F., 1985. Solubilities of chlorofluorocarbons 11 and 12 in water and seawater. Deep Sea Res. Part Oceanogr. Res. Pap. 32, 1485–1497.

Waugh, D.W., Haine, T.W.N., Hall, T.M., 2004. Transport times and anthropogenic carbon in the subpolar North Atlantic Ocean. Deep Sea Res. Part Oceanogr. Res. Pap. 51, 1475–1491. doi:10.1016/j.dsr.2004.06.011

Waugh, D.W., Hall, T.M., McNeil, B.I., Key, R., Matear, R.J., 2006. Anthropogenic CO_2 in the oceans estimated using transit time distributions. Tellus B 58, 376–389. doi:10.1111/j.1600-0889.2006.00222.x

Zeebe, R.E., 2012. History of Seawater Carbonate Chemistry, Atmospheric CO_2, and Ocean Acidification. Annu. Rev. Earth Planet. Sci. 40, 141–165. doi:10.1146/annurev-earth-042711-105521

Zeebe, R., Wolf-Gladrow, D., 2001. CO_2 in seawater: equilibrium, kinetics, isotopes. Elsevier Science.

Appendix

Appendix A

Offsets of the crossovers for the calculated A_T and C_T during the 1993 cruise ($\mu mol \cdot kg^{-1}$).

Cruise (Expocode)	year	A_T	C_T
TTO/TAS Leg 3	1981	-0.2±3.9	-4.7±5.0
32OC133 A20) 1983	1983	0.8±1.8	
32OC202_1-2_(A16Nad-1988)	1988	0.2±2.1	
3230CITHER2 (WOCE A17-1994)	1994	-3.0±2.3	-3.2±2.7
06MT19940219 (WOCE AR04e)	1994	1.5±1.4	
316N142_3 (A15/1994)	1994	1.7±1.3	
35LU19950909 (WOCE AR04g)	1995	-0.4±2.8	0.2±4.5
33LK19960415 (WOCE AR04h/AR15)	1996	0.4±3.1	0.3±1.6
35TH19990712 (Equalant 99)	1999	-0.6±1.7	-5.0±4.1
06MT20020607	2002	2.0±1.1	
06MT20021013	2002	3.2±1.2	
33RO20030604 (A16N/2003)	2003	0.9±2.4	0.3±1.6
29HE20100405 (MOC2/2010)	2010	0.6±2.7	1.5±3.5
29HE20130320 (A17-2013)	2013	0.0±1.2	
weighted average		**0.8±1.8**	**-1.1±3.3**

Appendix B

1993 mean data. Mean values and standard errors of the mean (x ± ε) salinity, potential temperature (θ, ºC), A_T (µmol·kg^{-1}), C_T (µmol·kg^{-1}), C_{ant}-φC_T^0 (µmol·kg^{-1}) and C_{ant}-TTD (µmol·kg^{-1}) for 1993. The thickness (m) of each layer was computed as the averaged vertical distance between layers weighted by the distance between stations. An additional factor, shown in the first column, was applied so that each region had the same total depth as in the 2010 MOC2 cruise.

Region	Layer	Thickness	Salinity	Θ	A_T	C_T	C_{ant}-ϕC_T^0	C_{ant}-TTD
WB	**SACW**	143±12	36.315±0.022	25.18±0.32	2379±1	2050±6	53.4±0.7 (n=40)	54.2±0.6 (n=68)
1.012	**SAMW**	269±19	35.114±0.046	10.75±0.31	2315±2	2182±3	20.8±1.3 (n=28)	21.2±0.9 (n=53)
	AAIW	658±21	34.642±0.012	5.81±0.12	2303±1	2213±1	9.8±0.7 (n=40)	7.2±0.4 (n=78)
	uNADW	1167±59	34.980±0.009	4.06±0.07	2315±0	2166±1	8.9±0.3 (n=78)	8.5±0.2 (n=151)
	lNADW	1532±129	34.913±0.002	2.22±0.03	2326±0	2170±0	5.4±0.2 (n=69)	7.4±0.1 (n=133)
	AABW	156±18	34.877±0.002	1.75±0.01	2334±1	2183±2	4.8±0.4 (n=11)	7.3±0.1 (n=24)
WR	**SACW**	146±9	36.164±0.027	24.48±0.42	2369±2	2046±9	51.3±1.4 (n=27)	53.3±1.0 (n=60)
0.988	**SAMW**	347±10	34.973±0.027	9.89±0.21	2308±1	2193±3	18.8±0.9 (n=26)	18.0±0.7 (n=55)
	AAIW	579±12	34.688±0.006	5.83±0.10	2302±0	2218±1	6.2±0.9 (n=31)	5.0±0.3 (n=71)
	uNADW	1306±28	34.962±0.003	3.86±0.04	2318±0	2172±1	7.5±0.3 (n=107)	6.1±0.1 (n=217)
	lNADW	1709±63	34.908±0.001	2.24±0.02	2333±0	2179±1	5.9±0.1 (n=109)	5.1±0.1 (n=235)
	AABW	552±59	34.835±0.003	1.42±0.03	2348±1	2208±2	7.7±0.2 (n=38)	5.0±0.1 (n=70)
ER	**SACW**	103±6	36.014±0.035	22.67±0.62	2361±2	2058±13	52.5±1.0 (n=25)	48.2±1.5 (n=45)
0.988	**SAMW**	383±6	35.149±0.024	11.47±0.22	2314±1	2198±4	20.7±1.3 (n=28)	20.7±0.8 (n=56)
	AAIW	573±7	34.694±0.007	5.83±0.12	2304±1	2225±1	6.1±0.7 (n=28)	4.1±0.2 (n=60)
	uNADW	1424±16	34.932±0.004	3.84±0.04	2321±0	2180±1	6.7±0.3 (n=102)	3.6±0.1 (n=206)
	lNADW	1927±103	34.900±0.001	2.18±0.02	2340±0	2189±1	6.5±0.1 (n=114)	3.3±0.0 (n=212)
EB	**SACW**	148±7	35.609±0.024	20.53±0.46	2335±2	2108±13	48.5±1.0 (n=48)	42.4±1.4 (n=70)
1.023	**SAMW**	338±9	35.182±0.021	11.61±0.23	2314±1	2215±4	22.1±1.3 (n=26)	18.4±1.0 (n=40)
	AAIW	588±7	34.718±0.005	5.88±0.11	2306±1	2234±2	6.4±0.7 (n=27)	3.6±0.2 (n=49)
	uNADW	1251±54	34.922±0.003	3.78±0.04	2322±0	2192±1	7.2±0.3 (n=64)	2.6±0.1 (n=104)
	lNADW	1791±152	34.905±0.002	2.26±0.02	2345±1	2198±1	8.7±0.2 (n=60)	2.9±0.1 (n=109)

Appendix C

2010 mean data. Mean values and standard errors of the mean (x ± ε) salinity, potential temperature (θ, ºC), A_T (µmol·kg^{-1}), C_T (µmol·kg^{-1}), C_{ant}-φC_T^0 (µmol·kg^{-1}) and C_{ant}-TTD (µmol·kg^{-1}) for 2010. The thickness (m) of each layer was computed as the averaged vertical distance between layers weighted by the distance between stations.

Region	Layer	Thickness	Salinity	Θ	A_T	C_T	C_{ant}-ϕC_T^0	C_{ant}-TTD
WB	**SACW**	168±8	36.098±0.029	25.48±0.45	2365±2	2040±7	69.8±0.7 (n=74)	72.0±1.7 (n=26)
	SAMW	290±17	34.974±0.036	10.02±0.25	2308±2	2192±2	31.0±0.9 (n=49)	27.9±1.6 (n=18)
	AAIW	564±21	34.645±0.007	5.96±0.12	2300±1	2219±1	15.5±0.8 (n=56)	8.3±0.6 (n=32)
	uNADW	1162±62	34.944±0.009	4.23±0.11	2314±0	2179±3	10.9±0.4 (n=44)	11.0±0.6 (n=31)
	lNADW	1581±83	34.916±0.003	2.30±0.05	2324±1	2172±1	7.3±0.2 (n=45)	10.7±0.3 (n=33)
	AABW	161±14	34.867±0.004	1.70±0.03	2338±1	2191±2	7.2±0.3 (n=6)	9.0±0.4 (n=5)
WR	**SACW**	148±4	36.064±0.015	24.95±0.36	2363±1	2052±6	64.7±1.2 (n=105)	72.3±1.5 (n=42)
	SAMW	349±10	35.013±0.018	10.37±0.14	2309±1	2195±2	31.9±0.7 (n=132)	26.7±1.1 (n=39)
	AAIW	600±10	34.700±0.005	6.15±0.10	2302±0	2225±1	14.8±0.5 (n=101)	7.6±0.5 (n=61)
	uNADW	1160±20	34.946±0.006	4.16±0.07	2316±0	2180±2	10.6±0.3 (n=76)	8.9±0.4 (n=48)
	lNADW	1881±63	34.915±0.002	2.35±0.04	2329±0	2177±1	7.7±0.1 (n=98)	7.3±0.2 (n=61)
	AABW	502±33	34.827±0.003	1.38±0.03	2348±1	2210±1	8.8±0.2 (n=33)	6.7±0.1 (n=19)
ER	**SACW**	127±5	35.815±0.021	21.65±0.60	2349±1	2106±10	63.5±1.2 (n=74)	61.1±2.9 (n=21)
	SAMW	363±15	35.138±0.017	11.47±0.17	2314±1	2204±3	34.4±0.8 (n=89)	27.6±2.4 (n=18)
	AAIW	610±13	34.718±0.009	6.24±0.15	2304±0	2234±1	14.8±0.6 (n=62)	6.6±0.6 (n=33)
	uNADW	1179±33	34.926±0.008	4.06±0.08	2317±0	2187±2	9.2±0.3 (n=46)	5.2±0.4 (n=25)
	lNADW	2131±115	34.906±0.002	2.27±0.04	2337±1	2188±1	7.7±0.1 (n=73)	3.9±0.2 (n=38)
EB	**SACW**	192±7	35.609±0.014	20.50±0.81	2338±2	2124±18	61.2±1.6 (n=38)	59.6±4.1 (n=15)
	SAMW	268±9	35.209±0.030	11.82±0.33	2316±1	2229±4	35.0±1.9 (n=19)	33.7±1.5 (n=8)
	AAIW	644±5	34.733±0.011	6.33±0.19	2305±1	2242±2	15.2±0.9 (n=26)	5.6±0.6 (n=22)
	uNADW	1035±111	34.912±0.010	3.95±0.12	2320±1	2196±3	7.8±0.3 (n=17)	3.2±0.6 (n=15)
	lNADW	1978±230	34.905±0.005	2.28±0.07	2343±2	2197±2	8.2±0.3 (n=21)	2.4±0.2 (n=20)